Cancer Cell

Article

Depletion of an immature cord blood NK subset reverses trogocytosis-driven CAR NK dysfunction

Graphical abstract

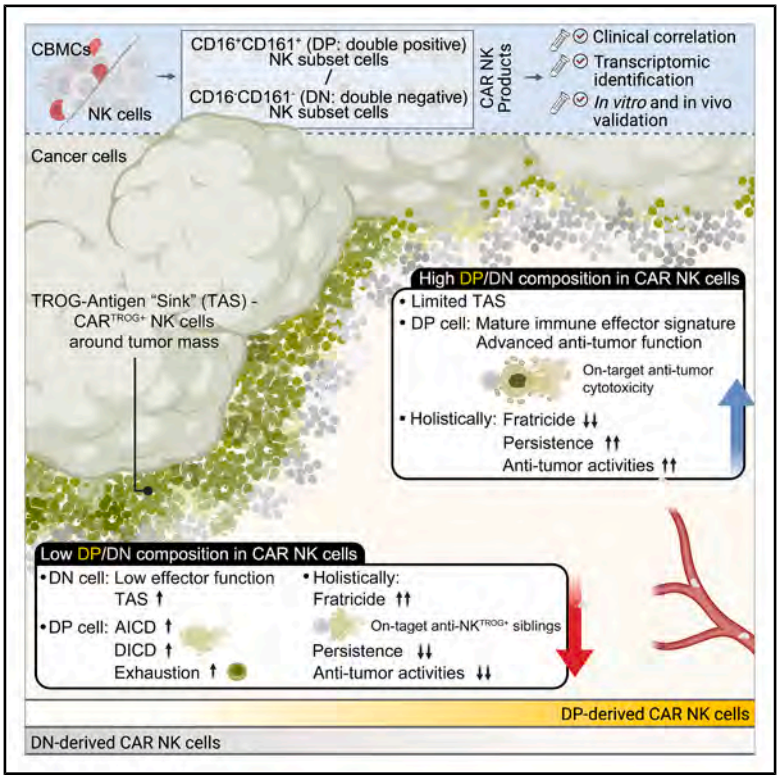

Highlights

- Cord blood donor composition determines CAR NK potency and persistence
- Immature DN NK cells drive excessive trogocytosis (TROG) after CAR engineering
- DN-driven TROG-antigen sink causes fratricide, AICD, and exhaustion of DP CAR NK cells
- DN depletion removes TROG-antigen sink and improves CAR NK persistence and tumor control

Authors

Ye Li, Huihui Fan, Guohui Wang, ..., Navin Varadarajan, Elizabeth J. Shpall, Katayoun Rezvani

Correspondence

yli55@mdanderson.org (Y.L.), krezvani@mdanderson.org (K.R.)

In brief

Li et al. identify a previously unrecognized NK cell subset that limits cord blood-derived CAR-NK cell therapy by diverting tumor targeting and promoting self-directed fratricide and show that donor cell composition shapes efficacy while offering a practical manufacturing strategy to improve consistency, persistence, and antitumor activity of off-the-shelf CAR-NK therapies.

Li et al., 2026, Cancer Cell *44*, 1–16
September 14, 2026
https://doi.org/10.1016/j.ccell.2026.06.017

CellPress

Please cite this article in press as: Li et al., Depletion of an immature cord blood NK subset reverses trogocytosis-driven CAR NK dysfunction, Cancer Cell (2026), https://doi.org/10.1016/j.ccell.2026.06.017

Cancer Cell

CellPress
OPEN ACCESS

Article

Depletion of an immature cord blood NK subset reverses trogocytosis-driven CAR NK dysfunction

Ye Li,[1,2,*] Huihui Fan,[1,2] Guohui Wang,[1,2] Xin Wang,[1,2] Rafet Basar,[1,2] Maliha Nuzhat Munir,[1,3] Nadima Uprety,[1,2] Rejeena Shrestha,[1,2] Ludovica La Posta,[4,5] Bin Liu,[1,2] Jeffrey Wilson,[1] Prashant Menon,[6] Natalie Wall Fowlkes,[1,2] Patrick Zhang,[1,2] Enli Liu,[1,2] Gary M. Deyter,[1,2] Luis Muniz-Feliciano,[1,2] Pinaki P. Banerjee,[1] May Daher,[1,2] David Marin,[1] Eleonora Dondossola,[5] Navin Varadarajan,[6] Elizabeth J. Shpall,[1] and Katayoun Rezvani[1,2,7,*]

[1]Department of Stem Cell Transplantation and Cellular Therapy, The University of Texas MD Anderson Cancer Center, Houston, TX, USA
[2]Institute for Cell Therapy Discovery and Innovation, The University of Texas MD Anderson Cancer Center, Houston, TX, USA
[3]UTHealth Graduate School of Biomedical Sciences, The University of Texas MD Anderson Cancer Center, Houston, TX, USA
[4]Department of Bioengineering, Rice University, Houston, TX, USA
[5]Department of Genitourinary Medical Oncology, David H. Koch Center for Applied Research of Genitourinary Cancers, The University of Texas MD Anderson Cancer Center, Houston, TX, USA
[6]Department of Chemical and Biomolecular Engineering, University of Houston, Houston, TX, USA
[7]Lead contact
*Correspondence: yli55@mdanderson.org (Y.L.), krezvani@mdanderson.org (K.R.)
https://doi.org/10.1016/j.ccell.2026.06.017

SUMMARY

Allogeneic CAR-engineered NK cells enable scalable off-the-shelf therapy, yet donor heterogeneity remains a major barrier to consistent potency. Building on our clinical experience with cord blood-derived CAR NK cells, we identified an immature $CD16^{-}CD161^{-}$ double-negative (DN) NK subset associated with poor outcomes. Following CAR engineering, DN-derived NK cells remained hypofunctional yet exhibited exaggerated trogocytosis, accumulating high levels of cognate antigen and forming an intra-product trogocytic-antigen sink (TAS) that diverted CAR engagement from tumor targets and promoted on-target off-tumor interactions within the product. Consequently, $CD16^{+}CD161^{+}$ double-positive (DP) effectors exposed to the TAS underwent sustained activation, metabolic stress, fratricide, reduced viability, programmed cell death, and progressive exhaustion, culminating in impaired persistence and tumor control. Pre-manufacturing DN depletion eliminated the TAS and restored DP antitumor activity across hematologic and solid tumor models. Together, these findings define a donor subset-driven mechanism of CAR NK dysfunction and provide a manufacturing strategy to improve antitumor potency.

INTRODUCTION

Adoptive cellular therapy with chimeric antigen receptor (CAR) T cells has transformed the treatment of hematological malignancies, yet broad implementation remains limited by manufacturing scalability, cost, and toxicity management.[1–3] Natural killer (NK) cells offer a promising allogeneic platform because they can be given without HLA matching, enabling truly off-the-shelf therapy without the risk of graft-versus-host disease.[4–7] However, a practical barrier to standardization is donor-to-donor variability, where a suboptimal source unit can translate into inconsistent expansion, persistence, and tumor control.[8]

We previously reported a phase 1/2 clinical trial of cord blood (CB)-derived CAR19/IL-15 NK cells in heavily pretreated patients with CD19-positive B cell lymphoid malignancies (NCT03056339), demonstrating clinical activity with limited toxicity.[8,9] Because each patient received a product manufactured from a distinct banked CB unit, this study provided a direct opportunity to distinguish optimal versus suboptimal cords and to define the underlying biology driving these donor effects.[8]

Here, we show that CAR NK cell performance was strongly shaped by the balance between two CB-NK cell subsets defined by CD16 and CD161 expression, and we identified an actionable strategy to improve suboptimal CB donors. After expansion and CAR engineering, cells derived from the immature $CD16^{-}CD161^{-}$ double-negative (DN) subset were hyporesponsive as direct tumor killers but exhibited exaggerated trogocytosis (TROG), accumulating high levels of cognate tumor antigen on their surface, a process further amplified by CAR signaling.[10,11] In mixed CB-NK cell products with a substantial DN fraction, this trogocytic antigen pool redirected CAR engagement into on-target off-tumor interactions within the product, limiting effective tumor-directed killing and imposing sustained activation

Please cite this article in press as: Li et al., Depletion of an immature cord blood NK subset reverses trogocytosis-driven CAR NK dysfunction, Cancer Cell (2026), https://doi.org/10.1016/j.ccell.2026.06.017

pressure on the $CD16^{+}CD161^{+}$ double-positive (DP) effector compartment. As a result, otherwise cytotoxic DP-derived CAR NK cells underwent prolonged antigen exposure and activation-induced cell death (AICD), fratricide, and progressive dysfunction, culminating in reduced persistence and loss of tumor control. By contrast, products enriched for DP cells showed superior cytotoxicity and persistence in multiple *in vitro* and *in vivo* tumor models. Finally, we demonstrated that depleting DN cells before engineering was sufficient to prevent these interactions and to convert suboptimal donors into consistently potent products, supporting subset profiling and DN depletion as a practical intervention to improve the consistency and potency of CAR NK cell therapy.

RESULTS

Pre-expansion CB-NK subset composition determined CAR19/IL-15 efficacy and clinical outcome

We recently reported a first-in-human phase 1/2 clinical trial (NCT03056339), in which each patient received a CAR19/IL-15 NK cell product manufactured from a distinct banked CB unit.[8] To link donor composition to clinical outcome, we profiled unmanipulated NK cells from residual reference vials through mass cytometry (CyTOF, cytometry by time of flight) and single-cell clustering (Figures 1A–1C; Figure S1A). Spanning-tree progression analysis of density-normalized event (SPADE) identified five NK cell clusters (C1-1 to C1-5). A mature, cytotoxic cluster (C1-1) was enriched in source units for responders and expressed CD16, CD161, NKG2D, KIRs, and NKp46, together with the transcription factors EOMES and T-bet, high levels of perforin (PFN), and granzyme B (GrB; Figures 1B and 1C). In contrast, source units from non-responders were enriched for an immature cluster (C1-5), with low or absent expression of key receptors and uniformly low maturation, homing, activation, and cytotoxicity scores (Figures 1B and 1C).

To classify these populations through a simple and biologically relevant gate, we stratified CB-NK cells by surface CD16 and CD161 expression, two markers that define NK cell maturation and effector competence. CD16 (Fc-γRIIIa) is acquired with terminal differentiation and is linked to antibody-dependent cellular cytotoxicity (ADCC) and the cytotoxic $CD56^{dim}$ program.[12–14] CD161 (KLRB1) increases with maturation and, in our dataset, co-segregated with canonical NK cell effector and homing receptors, including KIRs, NKp46, NKG2D, and CX3CR1.[7,14–16] Using this definition, the DP $CD16^{+}CD161^{+}$ cells corresponded to the mature C1-1 cluster, whereas the DN $CD16^{-}CD161^{-}$ subset was enriched in the immature C1-5 population (Figures 1B and 1C; Figure S1B). A higher DP/DN ratio in the source CB unit correlated with higher response rates and longer survival following CAR NK cell infusion (Figures 1D–1F). Collectively, these findings showed that pre-expansion NK cell composition of the CB source unit predicts CAR19/IL-15 product potency and clinical outcome.

Transcriptomic profiling defines immature and effector CB-NK cell states

To further define these subsets, we profiled the transcriptomic signatures of pre-expansion CB-NK cells used for CAR NK cell manufacturing (Figure 2A). Single-cell RNA sequencing (scRNA-seq) identified five NK cell clusters (CBNK-C1 to CBNK-C5), distinguished by their transcriptomic profiles and by the expression of *FCGR3A* and *KLRB1*, which encode CD16 and CD161 (Figures 2B and 2C; Figure S2). CBNK-C1 cells lacked both *FCGR3A* and *KLRB1* but expressed a high level of *NCAM1* (CD56), consistent with an immature DN state. Differentiation trajectory analysis projected progression from CBNK-C1 toward the $FCGR3A^{+}/KLRB1^{+}$ clusters, CBNK-C4 and CBNK-C5 (Figure 2D).

Pseudotime analysis further demonstrated that along this trajectory, immune effector potential increased with higher expression of *PRF1*, *GZMA*, *GZMH*, and *GZMB* in CBNK-C4 without increased expression of exhaustion or checkpoint markers (e.g., *LAG3*, *HAVCR2*, *TIGIT*, and *PDCD1*; Figures 2D and 2E). This profile was consistent with the mature DP phenotype identified by CyTOF. By contrast, cytotoxic molecule expression declined in the later pseudotime projected CBNK-C5 cluster (Figures 2D and 2E).

At the gene expression level, CBNK-C1 (DN) cells expressed genes associated with development and differentiation, including *RORA*,[17,18] *RUNX1*,[19] and *MAPK1*,[20,21] but had low expression of canonical NK cell receptors such as *NCR2*, *NCR3*, *KLRK1*, and *KLRC2* (Figure 2F). Together with low cytotoxic molecule expression, these findings indicate reduced cytotoxic and activation potential in CBNK-C1 cells, which increased as cells acquired *KLRB1* and/or *FCGR3A* expression across CBNK-C2 to CBNK-C5 (Figure 2F). Pathway analysis further demonstrated an early differentiation state in CBNK-C1 cells, with increased biosynthetic activity, mitotic remodeling, and metabolic fitness (Figures 2G and 2H).

Although all CB-NK cell clusters showed some immune response potential, CBNK-C5 showed increased apoptosis and hypoxia signatures, including *HSPA9*,[22] *BCL2L11*,[23,24] *APOL6*,[23,24] and *BCL6*,[23,24] suggesting impaired cell viability and reduced functional persistence during manufacturing (Figures 2F–2H). Together, these data identify an immature NK cell subset (DN; CBNK-C1) in pre-expansion CB-NK cells, while the strongest effector potential is retained by DP cells within CBNK-C4.

Single-cell analysis revealed distinct functional programs in NK cells expanded from DP and DN subsets

Functional studies showed that DP- and DN-NK cell subsets were not equivalent after expansion. DP-NK cells acquired a highly polyfunctional phenotype and showed enhanced antitumor activity after cytokine preactivation, whereas DN cells displayed delayed and weaker immune responses, including after *ex vivo* expansion and challenge with oncolytic virus-infected target cells (Figure S3). To further elucidate the molecular basis underlying these functional differences, we integrated scRNA-seq with matched surface antibody profiling of NK cells expanded from flow-sorted DP or DN subsets (Figure 3A). This approach allowed us to link subset of origin to the transcriptional and surface protein programs that emerged after expansion and to identify features most relevant for improved CAR signaling.

After two weeks of *ex vivo* expansion, the two products remained molecularly distinct (Figure S4A). DP-derived NK cells segregated into five transcriptional clusters (DP^{EX}-C1 to DP^{EX}-C5) while DN-derived cells resolved into nine clusters (DN^{EX}-C1 to DN^{EX}-C9; Figure 3B; Figures S4B, and S4C), indicating

Please cite this article in press as: Li et al., Depletion of an immature cord blood NK subset reverses trogocytosis-driven CAR NK dysfunction, Cancer Cell (2026), https://doi.org/10.1016/j.ccell.2026.06.017

CellPress
OPEN ACCESS

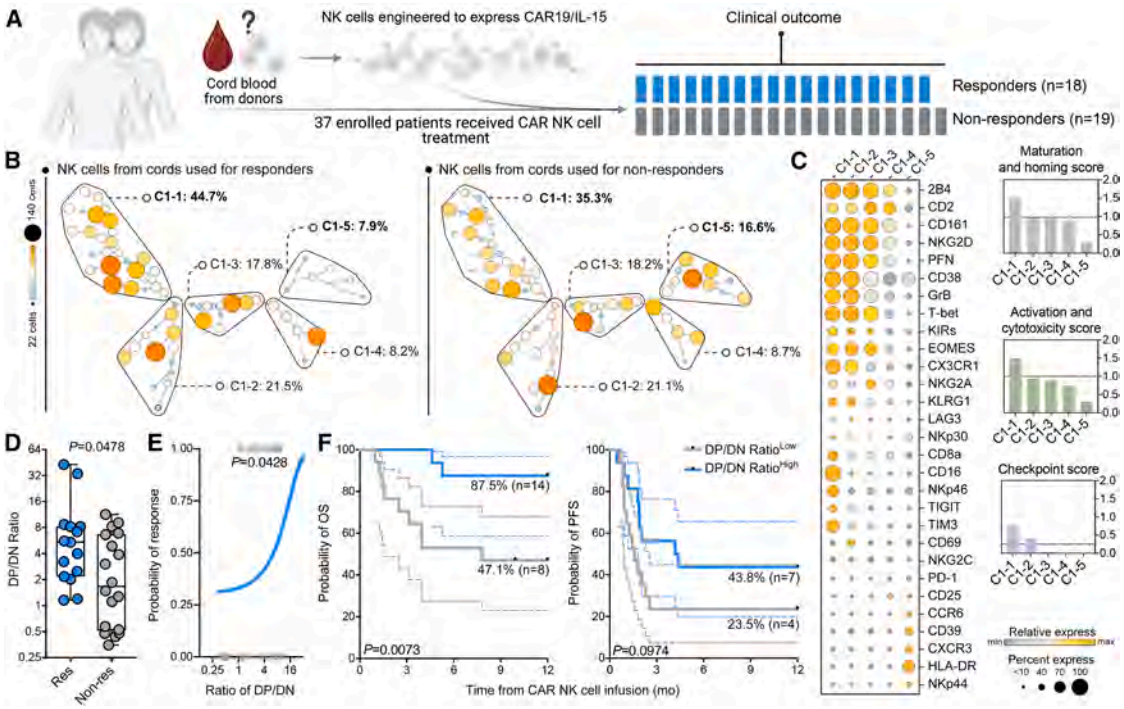

Figure 1. Donor cord blood NK cell phenotype and DP/DN ratio correlate with clinical benefit to CAR19/IL-15 NK cell therapy

(A) Schematic overview of the phase 1/2 clinical trial evaluating CAR19/IL-15 NK cell therapy in patients with B cell lymphoid malignancies (ClinicalTrials.gov: NCT03056339).

(B) Mass cytometry (CyTOF) profiling of unmanipulated donor CB-NK cells ($CD56^{+}CD3^{-}$) used to manufacture CAR19/IL-15 NK products for treated patients, grouped by clinical response; responders (n = 15 patients) and non-responders (n = 18 patients). Only samples with viable cord blood mononuclear cells (CBMCs) > 1,500 were included. Each cluster is represented as a node, where size and color indicate the frequency and abundance of NK cells within that cluster.

(C) Heatmap of marker expression across NK cell clusters. Percentage expression was determined using fluorescence-minus-one (FMO) controls and reference to negative lineages in CBMCs. Functional scores for maturation/homing, activation/cytotoxicity, and immune checkpoint expression were calculated from normalized marker intensities. Dashed gray lines indicate dataset medians. PFN, perforin; GrB, granzyme B.

(D) Bar graph showing the ratio of double-positive (DP; cluster C1-1: $CD16^{+}CD161^{+}$) to double-negative (DN; cluster C1-5: $CD16^{-}CD161^{-}$) NK subsets in unmanipulated donor CB-NK cells used to manufacture CAR19/IL-15 NK products. Ratios (n = 33 donors) ranged from 0.35 to 42.87 (median: 3.23). Data are shown as box and whiskers (min to max) with each symbol representing the infused product for an individual patient, grouped by clinical response (responder versus non-responder). p value determined by two-tailed Mann-Whitney test.

(E) Non-linear regression analysis correlating DP/DN ratios in CB-NK cells with clinical response to CAR NK treatment. p value determined by likelihood-ratio test.

(F) Kaplan-Meier survival curves for overall survival (OS; left) and progression-free survival (PFS; right) in patients stratified by the DP/DN ratio of the donor NK cells used to generate their personalized CAR NK cell products. High (>median; n = 16 donors) and low (≤median; n = 17 donors) DP/DN ratio groups are shown. Tick marks indicate censored patients. Regions between dashed lines represent 95% confidence intervals. p values determined by log rank test.

greater heterogeneity in the DN-derived product. Surface protein profiles mirrored these differences. DP-derived cells largely maintained co-expression of $CD56^{dim}$, CD16 and CD161, while DN-derived NK cells remained predominantly $CD56^{hi}$ with only partial acquisition of CD16 and/or CD161 (Figure 3C). Consistent with this phenotype, DP-derived NK cells enriched for cytotoxic and activated states, including DP^{EX}-C1 (49.7%) and DP^{EX}-C2 (11.2%) clusters, as well as proliferative states including DP^{EX}-C4-*MKI67* (33.5%) and DP^{EX}-C5-*MKI67* (5.2%) clusters (Figures 3D and 3E). By contrast, expanded DN-derived NK cells distributed across multiple states (Figure 3D), contributing comparably to three proliferative clusters characterized by high *MKI67* expression: DN^{EX}-C7-*MKI67* (24.4%), DN^{EX}-C8-*MKI67* (4.1%), and DN^{EX}-C9-*MKI67* (8.0%; Figures 3D and 3E) with weaker maturation features.

Because proliferation can obscure functional interpretation, we evaluated cycling and non-cycling compartments separately. Cell cycle phase distributions were broadly similar between DP- and DN-derived expanded NK cells (Figure S4D). Cycling cells from both origins showed inflammatory and anti-viral programs with RAS and NF-κB signaling[25] (Figure S4E). Notably, DP-derived cycling NK cells scored higher for activation, with signatures dominated by membrane-proximal signaling, whereas DN-derived cycling cells showed relatively greater reliance on endosomal activation pathways (Figure S4F).

We next focused on non-cycling cells to define effector programs independent of cell cycle (Figure 3F; Figures S5A–S5C). DP-derived non-cycling NK cells retained a coordinated mature cytotoxic architecture, including high expression of natural cytotoxicity receptors (NCRs: *NCR1*, *NCR2*, *NCR3*, and *KLRD1*), membrane-proximal signaling adaptors (*ZAP70*, *CD247*, *SYK*, and *CD244*), and cytotoxic effector genes (*PRF1*, *FCGR3A*, *FCGR3B*, and *KLRF1*; Figure 3F), with the strongest enrichment in the DP^{EX}-C2 cluster. This cluster also showed higher

Please cite this article in press as: Li et al., Depletion of an immature cord blood NK subset reverses trogocytosis-driven CAR NK dysfunction, Cancer Cell (2026), https://doi.org/10.1016/j.ccell.2026.06.017

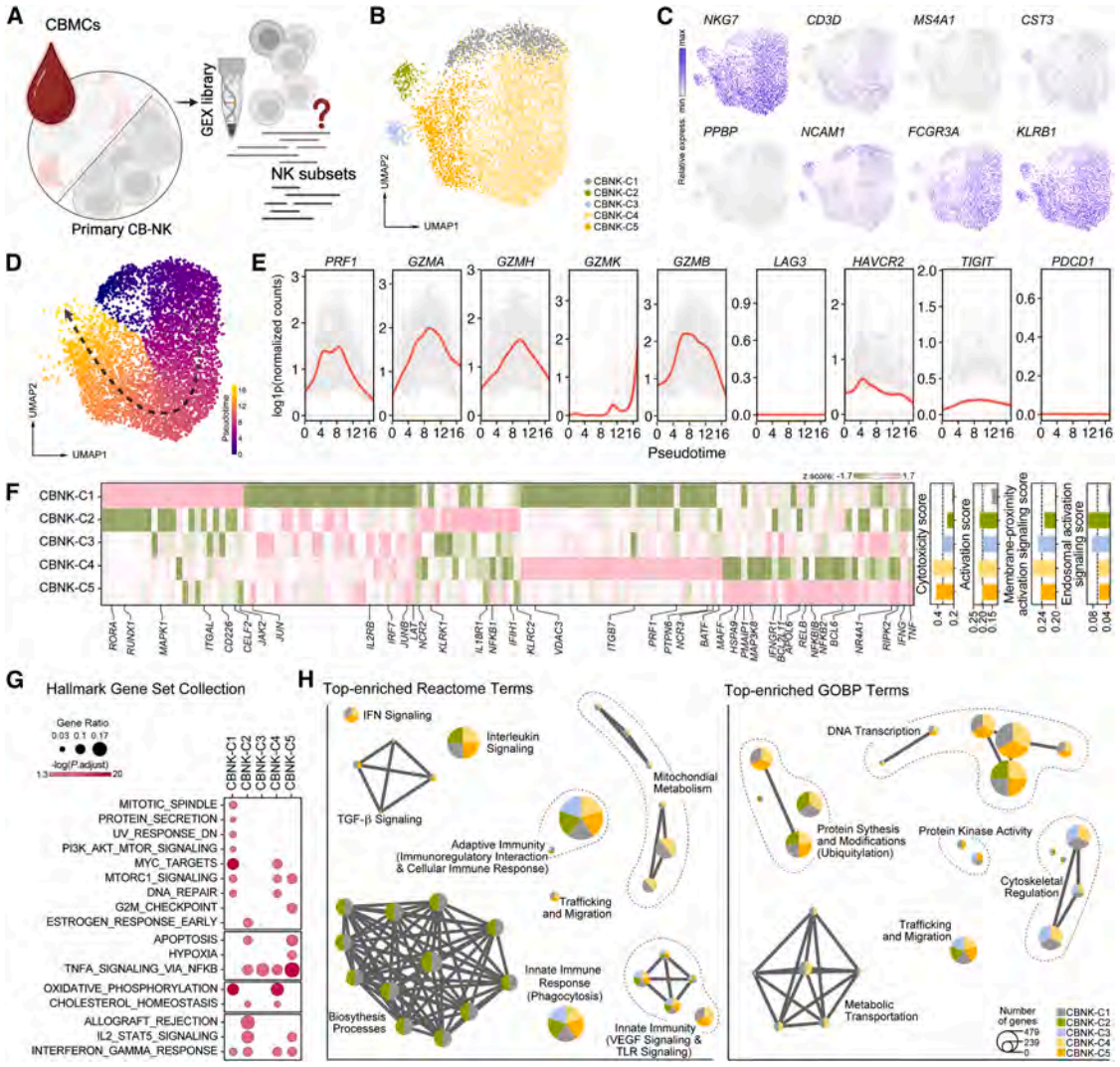

Figure 2. Transcriptomic profiling defines immature and effector CB-NK cell states before expansion

(A) Workflow for single-cell transcriptomic profiling of pre-expansion CB-NK cells used for CAR19/IL15 NK cell manufacturing from four donors.

(B) Uniform manifold approximation and projection (UMAP) visualization of five transcriptionally distinct CB-NK cell clusters, annotated based on differentially or highly expressed genes associated with NK cell functional states.

(C) Density of UMAP plots showing immune lineage markers *NKG7*, *CD3D*, *MS4A1*, *CST3*, *PPBP*, and *NCAM1*, together with *FCGR3A* and *KLRB1*, which define DP- and DN-NK cell subsets.

(D) UMAP plot showing pseudotime trajectories from DN-NK C1 cells toward DP-NK C4 and C5 clusters.

(E) Line plots showing expression of selected genes along the pseudotime trajectory, including markers of cytotoxic function and checkpoint regulation.

(F) Expression patterns of functional genes in CB-NK cell clusters, with AUCell-based functional gene signature scores shown as bar plot on the right. Vertical dashed lines indicate median scores. Color scale indicates normalized expression *Z* score (green, low; pink, high), and square size reflects the magnitude of expression differences (*Z* score range: −1.7 to 1.7).

(G and H) Gene set enrichment analysis of cluster marker genes using (G) the hallmark gene set, (H) reactome (left), and Gene Ontology (GO) terms (right). *p* values were calculated by one-sided hypergeometric test and adjusted for false discovery rate (FDR).

expression of apoptosis-associated signaling genes including *CASP8*[26] and *TRADD*[27]; Figure 3F). In contrast, DN-derived NK cells favored transcriptional programs linked to trafficking (*ITGA1*, *CCR2*, and *CXCR3*) and innate anti-viral and pro-inflammatory responses (*MX1*, *IL18R1*, *TNFSF10*, and *CSF2RB*; Figure 3F).[28,29] A DN^{EX}-C3 cluster co-expressed multiple checkpoint receptors (*HAVCR2*, *LAG3*, *LILRB1*, and *PDCD1*), consistent with an early exhausted-like program in a minority of cells (4.7%; Figures 3F; Figures S5A and S5E). Endosomal and TLR-associated signaling signatures (*STING1*, *PRKCD*, and *SASH1*)[29–31] were also enriched in non-cycling DN cells (Figure 3F; Figures S5D–S5F). Although acquisition of CD16 and/or CD161 in DN-derived cells was associated with increased cytotoxicity and activation linked to membrane-proximal signaling, these programs remained weaker than those observed in DP-derived NK cells, a pattern that was mirrored within the cycling

Please cite this article in press as: Li et al., Depletion of an immature cord blood NK subset reverses trogocytosis-driven CAR NK dysfunction, Cancer Cell (2026), https://doi.org/10.1016/j.ccell.2026.06.017

CellPress
OPEN ACCESS

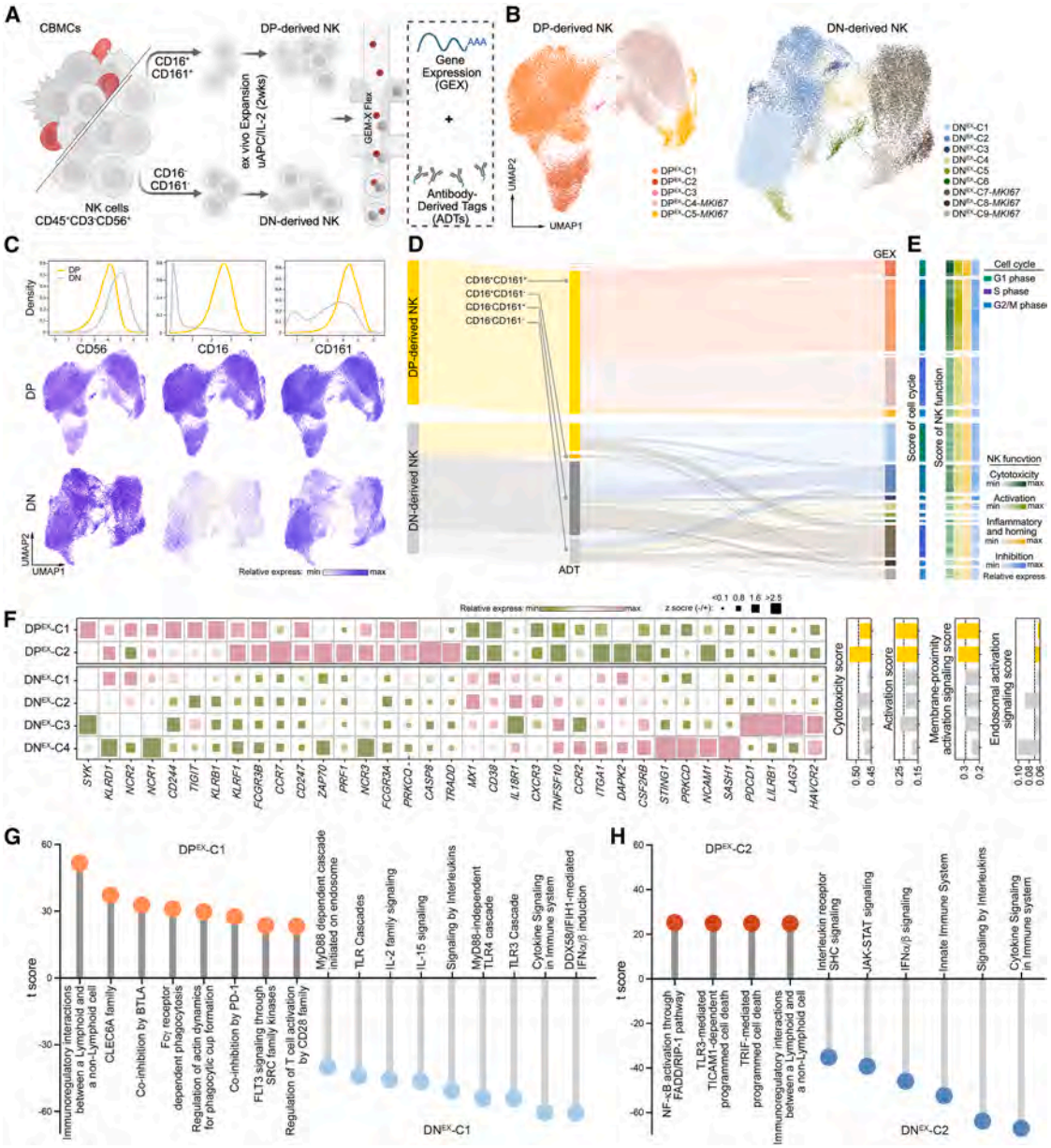

Figure 3. Transcriptional and proteomic characteristics of DP- and DN-derived NK subsets following *ex vivo* expansion

(A) Workflow for the purification, expansion, and single-cell profiling of CB-derived non-transduced (NT)-NK cell subset. $CD56^{+}CD3^{-}$ NK cells from an independent cohort of cord blood units (CBUs, $n = 6$ donors) were isolated and sorted based on surface expression of CD161 and CD16. $CD16^{+}CD161^{+}$ (DP) and $CD16^{-}CD161^{-}$ (DN) NK subsets were expanded for two weeks with uAPCs and exogenous IL-2 (200 U/mL; STAR Methods). Following expansion, cells were stained with nucleotide barcode-labeled antibodies, pooled at a 1:1 ratio, and profiled using the GEM-X Flex single-cell profiling kit.

(B) UMAP visualizations of DP-derived and expanded NK cells (DP^{EX}; left) or DN-derived and expanded NK cells (DN^{EX}; right). Clusters were annotated based on differentially/highly expressed genes associated with distinct NK cell functional states.

(C) Density and UMAP plots showing cell surface antigen levels of signature markers used to define DP- and DN-NK cell subsets at isolation, shown here in the corresponding expanded DP-derived and DN-derived populations.

(D) Sankey diagram illustrating the phenotypic trajectories of DP^{EX} and DN^{EX} cells across their isolated states/origin (left), cell surface protein-derived cell states (middle), and differentiated transcriptional functional states (right).

(E) Cell cycle annotation and AUCell scoring of NK cell functional gene signatures across individual cells. AUCell scores for each NK cell function are visualized per cell by using a color scale from minimum (bright) to maximum (dark) values.

(F) The expression patterns of functional genes in major DP^{EX} (upper) and DN^{EX} (lower) NK cell clusters (>2%; left), alongside the AUCell-based functional gene signature scores shown as bar plot with median scores as vertical dashed lines (right). Green-pink color scale indicates the *Z* score of normalized expression

(legend continued on next page)

Please cite this article in press as: Li et al., Depletion of an immature cord blood NK subset reverses trogocytosis-driven CAR NK dysfunction, Cancer Cell (2026), https://doi.org/10.1016/j.ccell.2026.06.017

compartment as well (DN^{EX}-C8-*MKI67*, 11.3% of DN-derived cycling NK cells; Figure 3F; Figures S4E and S5D–S5F). Direct comparison of the dominant clusters highlighted a consistent functional divergence, with DP-derived NK cells achieving the highest cytotoxicity and activation scores, whereas DN-derived cells were biased toward cytokine-driven and endosomal innate-sensing pathways (Figures 3G and 3H).

Together, these data provide a molecular basis for the distinct effector behavior of the two starting subsets after expansion. DP-derived NK cells preserve mature receptor and membrane proximal signaling networks that support potent cell-to-cell cytotoxicity.[4,7] DN-derived NK cells exhibit incomplete maturation and greater dependence on cytokine and endosomal-sensing pathways,[29–31] consistent with their relative hyporesponsiveness after CAR engineering as shown in Figure 4. Given that CAR activity depends heavily on effective membrane-proximal activation signaling through adaptor engagement and downstream cascades, these findings suggest intrinsic limitations of DN-derived cells as CAR vehicles relative to their DP-derived counterparts.

DN-derived CAR NK cells exhibit hyporesponsiveness despite *ex vivo* expansion

We next asked whether the NK cell subset of origin determines the functional competence after CAR engineering. CB-NK cells were enriched by $CD56^{+}CD3^{-}$ bead selection, flow-sorted into DP and DN subsets based on CD16 and CD161 expression, transduced with a CAR19/IL-15 vector, and expanded with uAPC feeder cells (STAR Methods). DN-derived CAR NK cells proliferated more slowly immediately after transduction, although this difference diminished after two expansion cycles (Figure 4A). Phenotypically, DP-derived CAR NK cells maintained high surface CD16 and CD161 expression (Figure 4B), whereas only a fraction of DN-derived cells acquired CD16 and/or CD161. Consistent with incomplete maturation, DN-derived CAR NK cells had reduced metabolic fitness, with impaired glycolysis and mitochondrial oxidative capacity (Figure S6A). They also showed reduced polyfunctionality after antigen stimulation, with reduced secretion of effector cytokines and chemokines and weaker cytotoxicity after repeated tumor challenge (Figures 4C and 4D).

To define the phenotypic states associated with these functional differences, we performed CyTOF profiling before and after tumor rechallenge (Figures 4E and 4F). When cultured without tumor, DP-derived CAR NK cells localized predominantly to a mature cluster (C4-1; 66.1%), characterized by high CD16, CD161, NKG2D, KIRs, and EOMES and high cytotoxic potential (Figures 4E and 4F). In contrast, DN-derived CAR NK cells only modestly upregulated maturation-associated receptors, and only a minority entered C4-1 (8.2%), with lower expression of CD16, CD161, NKG2D, CD95, KIRs, and EOMES (Figures 4E and 4F; Figure S6B). Following Raji rechallenge, DP-derived CAR NK cells retained superior antitumor activity and shifted into C4-2 (59.1%), a state closely related to C4-1 with minor antigen-induced reductions in CD16 and KIR expression (Figures 4E and 4F). In contrast, DN-derived CAR NK cells failed to control tumor effectively and accumulated almost entirely in C4-6 (96.9%), characterized by low maturation markers including CD16, CD161, KIRs, EOMES, and T-bet, together with reduced cytotoxic molecules including PFN and GrB (Figures 4E and 4F). Notably, after rechallenge, DN-derived cells upregulated activation-associated markers, including IL-2RA (CD25), CD39, CD69, and HLA-DR, without a dominant classical exhaustion phenotype (Figure 4F). Although their metabolic fitness after rechallenge was comparable to DP-derived cells (Figure S6C), their effector function remained blunted, consistent with a hyporesponsive state rather than terminal dysfunction.

We next evaluated antitumor activity under sustained tumor engagement using spheroid cocultures (Figure 4G). DP-derived CAR NK cells showed superior, dose-dependent antitumor activity relative to DN-derived cells; however, DP cells were progressively depleted during continued coculture. In contrast, DN-derived cells persisted and expanded over time *in vitro* (Figures 4G and 4H; Figure S6D). DP loss was most pronounced at low effector-to-target (E:T) ratios. At high E:T ratios, DP cell numbers declined early during active tumor engagement but began to expand after tumor clearance (Figures 4G and 4H). Consistent with this, prolonged tumor engagement and antigen exposure, most notably at low E:T conditions, significantly increased apoptosis in DP-derived CAR NK cells (Figure 4I) and coincided with markers of activation-induced cell death (AICD), including active caspase-8, Fas and FasL expression (Figures 4F and 4J),[32–36] as well as damage-induced cell death (DICD) pathways,[32,37] including pyroptosis with active caspase-1 expression (Figure 4J).[38] In contrast, DN-derived CAR NK cells were less susceptible to AICD and persisted longer but remained unable to achieve comparable tumor eradication.

Together, these data show that subset of origin imprints distinct post-engineering fates. DP origin supports mature receptor and signaling architecture that enable strong tumor control but comes at the cost of AICD under chronic antigen-driven stimulation. DN origin yields a more persistent product that remains functionally hyporesponsive despite expansion and antigen challenge.

DN-derived cells create a TROG-antigen sink that suppresses CAR NK cell function at the population level

CyTOF profiling after tumor challenge showed higher surface CD19 on DN-derived CAR NK cells than on DP-derived cells, consistent with greater trogocytic acquisition of cognate antigen and concomitant antigen stripping from tumor cells without efficient lysis (tCD19 shown in Figure 4F and functional data in Figures 5A and 5B). To test whether impaired effector function promotes trogocytic antigen accumulation, we used CRISPR-Cas9 to disrupt all three key cytotoxic mediators in CAR NK cells: *GZMB*, *PRF1*, and *IFNG*.[4,7] Similar to DN-derived CAR NK cells,

(green, low; pink, high), while square size is proportional to the magnitude of the *Z* score, with larger squares representing stronger expression differences (*Z* score thresholds: <0.1, 0.8, 1.6, and >2.5).

(G and H) Waterfall plots showing the differential immune functions enriched in (G) DP^{EX}-C1 versus DN^{EX}-C1 and in (H) DP^{EX}-C2 versus DN^{EX}-C1. Statistic t scores were determined by two-tailed Student's *t* test.

Please cite this article in press as: Li et al., Depletion of an immature cord blood NK subset reverses trogocytosis-driven CAR NK dysfunction, Cancer Cell (2026), https://doi.org/10.1016/j.ccell.2026.06.017

CellPress
OPEN ACCESS

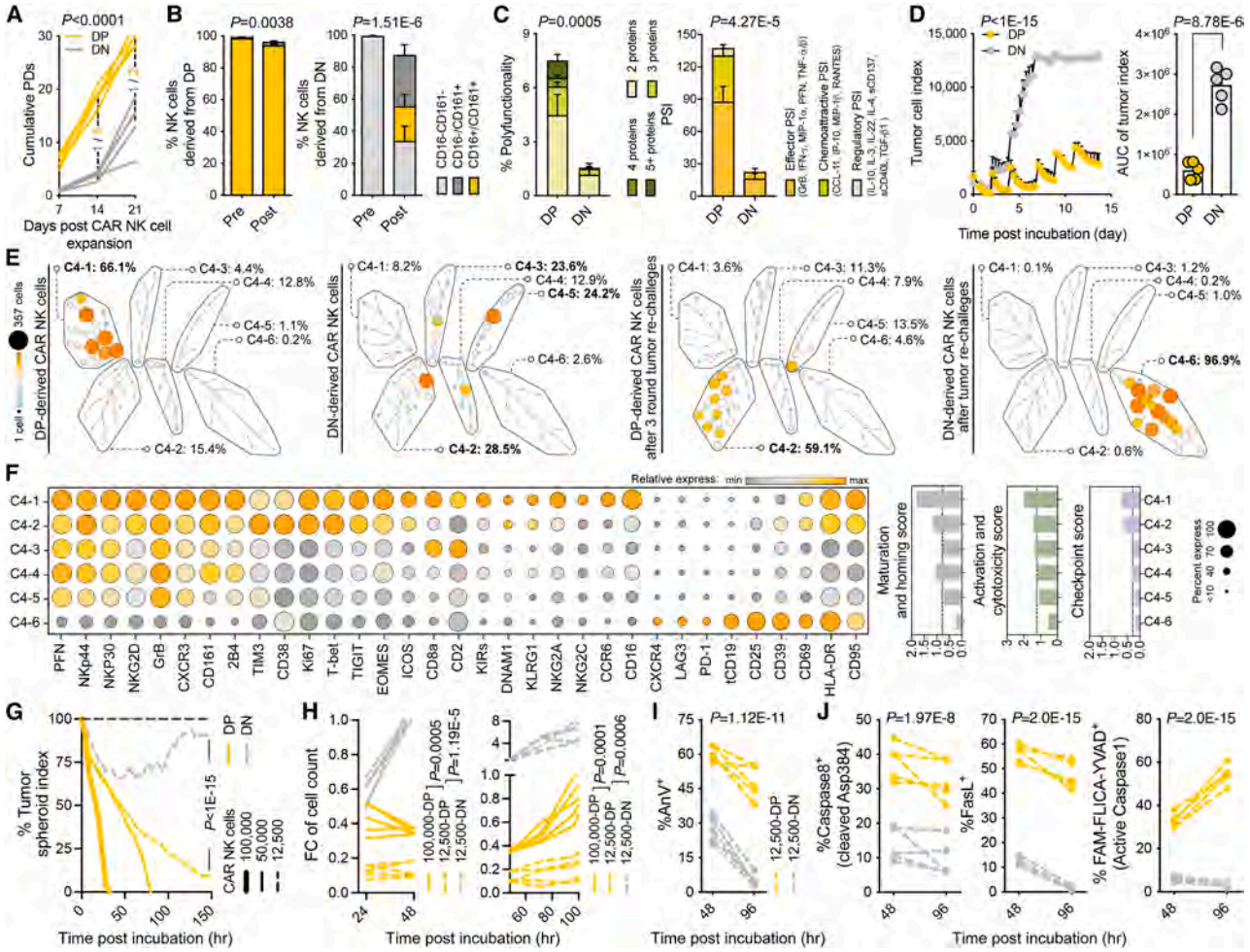

Figure 4. Antitumor immune effector functions of DP- and DN-derived CAR19/IL-15 NK cells

(A) Cumulative population doublings (PDs) during expansion of CAR19/IL-15 NK cells derived from DP or DN CB-NK subsets (n = 5 donors).

(B) Expression of CD16 and CD161 on DP- and DN-derived NK cells before and after CAR transduction and expansion (n = 5 donors).

(C) Bar graphs showing the percentage of polyfunctional cells and corresponding polyfunctionality strength index (PSI) of DP- or DN-derived CAR19/IL-15 NK cells (n = 3 donors) following CD19 antigen stimulation.

(D) Tumor rechallenge assay with DP- or DN-derived CAR19/IL-15 NK cells against Raji tumor cells. Bar graph shows area under the curve (AUC) of the tumor cell index (n = 5 donors).

(E) CyTOF profiling of CAR NK cells before and after the third Raji tumor cell challenge (n = 3 donors); cluster frequencies are indicated.

(F) Heatmap showing marker expression across clusters and corresponding functional scores. Dashed gray lines indicate dataset medians.

(G) Line graph showing percentage change in SKOV3^{gCD19+} spheroid index after co-culture with CAR NK cells derived from either DP or DN NK subset at various E:T ratios.

(H) Line graph showing the fold change (FC) of CAR NK cells after incubation with tumor spheroid in the early time (24-48 h; left) and in the later time (right).

(I and J) Line graph showing the positive percentage (%) of (I) Annexin V (AnV), (J) active form of caspase-8, FasL, and active form of caspase-1 on CAR NK cells derived from DP or DN NK subsets at the lower E:T ratio (seeding 12,500 CAR NK cells) overtime during the incubation with tumor.

p values were determined by two-tailed two-way ANOVA (A-D, G, and H), two-tailed Student's t test (bar graph; D), or two-tailed paired Student's t test (I and J). Data were assessed by flow cytometry (B) or CyTOF (E and F). Data were shown as mean + s.e.m; each symbol represents an individual donor.

effector-deficient CAR NK cells (CAR NK^{KO}) acquired high levels of tCD19 and stripped antigen from target tumors (Figures S7A and S7B).

Because TROG-antigen can decorate CAR effectors with target antigen and convert them into unintended targets for neighboring effectors,[10] we next asked whether disproportionate antigen uptake by DN-derived cells could alter the broader effector compartment. We defined a trogocytic-antigen sink (TAS) as transferred TROG-antigen expression that accumulates on CAR NK cell surfaces, generating competing cognate-expressing targets that divert effector activity away from tumor cells and toward fratricide and sustained activation, with downstream acceleration of AICD and exhaustion in otherwise potent DP-derived CAR NK effectors.

To directly measure killing kinetics, antigen uptake, and fratricide, we used a single-cell cytotoxicity assay in which sorted DP- or DN-derived CAR19/IL-15 NK cells were paired with an autologous NK sibling cell genetically engineered to express CD19

Please cite this article in press as: Li et al., Depletion of an immature cord blood NK subset reverses trogocytosis-driven CAR NK dysfunction, Cancer Cell (2026), https://doi.org/10.1016/j.ccell.2026.06.017

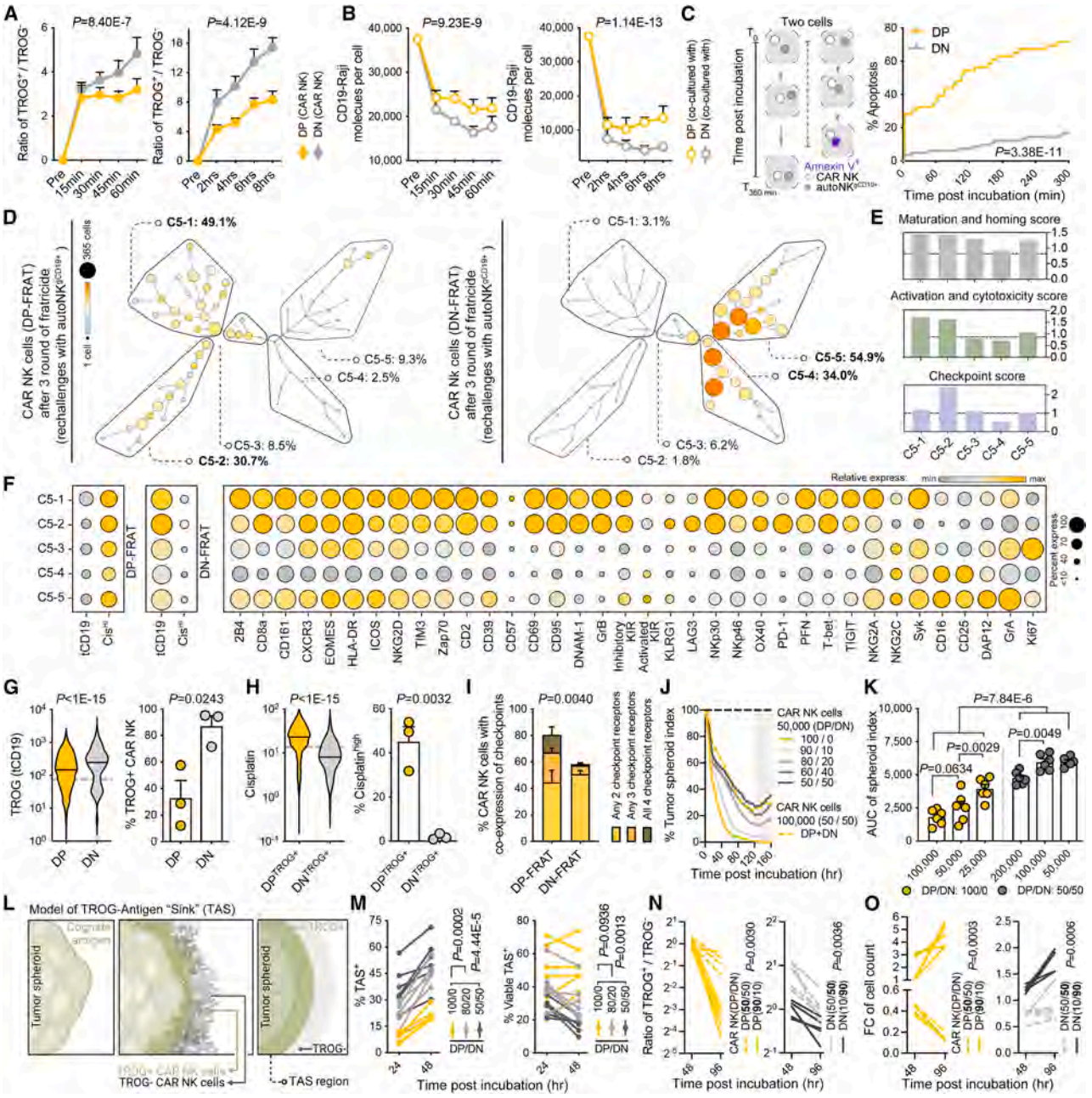

Figure 5. Effects of TROG-antigen expression on DP- and DN-derived CAR19/IL-15 NK cells on their antitumor activities

(A) TROG-acquired CD19 (tCD19) expression on singlet DP-derived (yellow) and DN-derived (gray) CAR19/IL-15 NK cells, shown as the ratio of $TROG^{+}$ to $TROG^{-}$ cells, assessed at early (0-60 min; left) and late (2-8 h; right) time points after co-culture with Raji targets (n = 3 donors).

(B) Quantification of CD19 molecules per Raji target cell after co-culture with DP- or DN-derived CAR19/IL-15 NK cells at early (0-60 min; left) and late (2-8 h; right) time points (n = 3 donors).

(C) Schematic of the single-cell cytotoxicity assay through DP- or DN-derived CAR19/IL-15 NK cells co-cultured with $autoNK^{gCD19+}$ targets (left). Kaplan-Meier survival curves show target cell apoptosis (right).

(D) CyTOF profiling of DP- and DN-derived CAR19/IL-15 NK cells after three rounds of fratricide challenge with $autoNK^{gCD19+}$ cells (n = 3 donors); cluster frequencies are indicated.

(E) Functional scores across five post-fratricide clusters. Dashed gray lines indicate dataset medians.

(F) Heatmap showing marker expression across post-fratricide clusters.

(G and H) Violin plots and bar graphs showing (G) TROG-acquired antigen (tCD19) expression and (H) CAR19/IL-15 NK cell viability after three rounds of fratricide challenge with $autoNK^{gCD19+}$ cells (n = 3 donors). Dashed lines indicate cutoffs based on marker expression in healthy NT-NK cells without co-culture.

(I) Bar graph showing co-expression of checkpoint molecules (PD-1, LAG3, TIM3, and TIGIT) in DP- versus DN-derived CAR NK cells after three rounds of fratricide challenge (FRAT) with $autoNK^{gCD19+}$ cells (n = 3 donors).

(legend continued on next page)

(autoNK^{gCD19+}; Figure 5C). DP-derived CAR NK cells killed CD19^{+} NK cell targets more rapidly than DN-derived effectors (Figure 5C), consistent with their superior antitumor function shown in Figure 4. Although target engagement frequencies were similar, DN-derived CAR NK cells required longer to complete killing (Figures S7C–S7E; Video S1).

CyTOF profiling after repeated cognate antigen-mediated fratricide revealed distinct phenotypic states in DP- and DN-derived CAR NK cells (Figure 5D). DP-derived effectors were enriched in C5-1 (49.1%) and C5-2 (30.7%), whereas DN-derived effectors were concentrated in C5-4 and C5-5 (88.9% in total; Figure 5D). DP-derived cells showed low tCD19 accumulation (Figures 5D–5G), but increased Fas (CD95) expression (Figure 5F), reduced viability with higher cisplatin uptake (Figures 5D–5F and 5H), increased exhaustion marker expression (Figures 5D–5F and 5I), and impaired oxidative phosphorylation and glycolytic function (Figures S7F and S7G). These features are consistent with activation-driven attrition under sustained CAR engagement.[10,39–41] By contrast, DN-derived effectors accumulated higher levels of tCD19 while maintaining viability and showed increased maturation, cytotoxicity, and activation features, particularly within C5-5 (54.9%; Figures 5D–5H).

We next tested whether DN origin could impair DP function at the population level by promoting TAS formation in mixed cultures. DP-derived CAR19/IL-15 NK cells were challenged with SKOV3 tumor spheroids engineered to express CD19 (SKOV3^{gCD19+}), while titrating in increasing proportions of DN-derived CAR19/IL-15 NK cells (Figure S8A). Increasing the DN fraction progressively reduced DP-mediated tumor clearance (Figures 5J and 5K; Figure S8A), whereas DP cells alone did clear spheroids efficiently, as we observed previously (Figure 4G). This suppressive effect was not observed in matched spheroids lacking cognate CD19, indicating antigen dependence (Figures S8B–S8D).

To visualize antigen redistribution and link it to functional impairment, we fused CD19 to mCherry (CD19^{mCherry}) and performed live cell imaging. In SKOV3^{gCD19+} spheroid cultures, increasing the DN fraction led to greater CD19$^{mCherry+}$ signal within the CAR NK cell population, consistent with the transfer of target antigen onto sibling CAR NK cells and TAS formation (Figure 5L; Figures S9A and S9B). Regions enriched for TAS showed increased fratricide and reduced tumor clearance within the same fields of view (Figure 5M; Figure S9C). Importantly, CAR NK cells with a low DP/DN ratio showed more prolonged exposure to TAS regions and reduced CAR cell persistence (Figures 5N and 5O; Figure S9D).

Together, these data support a model in which DN-derived CAR NK cells act as a sink for cognate antigen through enhanced TROG, redistributing antigen onto effector surfaces and generating TAS. This diversion of on-target interactions away from tumor cells toward fratricide and sustained activation promotes AICD and exhaustion in DP-derived effectors, thereby reducing overall antitumor efficacy.

Impaired *in vivo* antitumor activity of CAR NK cell products containing DN-derived NK cells

To test whether the TAS phenotype observed *in vitro* translates into loss of efficacy *in vivo*, we developed a dual tracking strategy to distinguish DP- and DN-derived effectors within the same infusion product. CB-NK cells were sort-purified into DN and DP subsets, and each subset was engineered to express a distinct CAR targeting either CD19 or CD20. In this setting, CAR-specificity served as an orthogonal lineage label rather than as a potency variable. *In vitro*, CAR19/IL-15 and CAR20/IL-15 NK cells showed comparable transduction efficiency, IL-15 expression and cytotoxicity against Raji targets, and each product acquired its respective cognate antigen, tCD19 or tCD20, together with additional membrane-associated molecules transferred by TROG (Figure S10).[10,11] This enabled us to use CAR19 and CAR20 as complementary lineage tags to track DP- and DN-derived effectors and quantify antigen transfer and sibling cell interactions in mixed cultures and *in vivo*.

In the Raji xenograft mouse model, we infused CAR NK cell products expanded from DN only, DP only, or mixed DP plus DN populations. Mixed infusion at a 4:1 DP/DN ratio failed to control tumor progression, and circulating CAR NK cells became rapidly dominated by DN-derived cells (peripheral blood [PB]; Figures S11A–S11E). To exclude an effect driven by the CAR target choice, we performed a reciprocal swap in which DN cells carried the alternate CAR and DP cells carried the other (Figure S11F). Mixed infusion again failed to control tumor growth and closely resembled the outcome of DN-only treatment (Figure S11G). Longitudinal tracking showed selective attrition of DP-derived CAR NK cells *in vivo* in both mixed groups, whereas DN-derived CAR NK cells persisted in PB (Figures S11C–S11E and S11H-S11J). By contrast, DP-only CAR NK cells achieved durable antitumor activity with superior *in vivo* persistence (Figures S11H–S11J).

Together, these findings show that inclusion of the DN subset in the CAR NK cell product compromises *in vivo* efficacy and drives preferential loss of DP-derived effectors, consistent with the *in vitro* model in which increased TROG-antigen acquisition by DN-derived cells promotes fratricide and activation-driven attrition within the effector compartment.

(J) Line graph showing percentage change in SKOV3^{gCD19+} spheroid index after co-culture with CAR NK cell products containing different DP/DN ratios.
(K) Area under the curve (AUC) of tumor spheroid index after incubation with DP-derived CAR NK cells at different E:T ratios, with or without addition of DN-derived CAR NK cells (n = 6 donors).
(L) Schematic illustrating the TROG-antigen sink (TAS) structure.
(M) Line graphs showing TAS positivity, defined by tCD19 expression, and viability of CAR NK^{TROG+} cells (n = 6 donors).
(N and O) Line graphs showing (N) the ratio of TROG-positive to TROG-negative cells, followed by (O) assessment of fold change (FC) of DP- and DN-derived CAR NK cells in mixtures with different DP/DN ratios. DN-derived NK cells expressed GFP to enable detection within mixed CAR NK cell products (n = 5 donors).
p values were determined by two-tailed two-way ANOVA (A and B), two-tailed Wilcoxon matched signed rank test (violin plot; G and H), two-tailed Student's t test (bar graph; G and H), two-tailed one-way ANOVA (K), or two-tailed paired Student's t test (M–O). Data were assessed through CyTOF (D–I) or flow cytometry (M–O). Data were shown as mean + SEM; each symbol represents an individual donor.

Please cite this article in press as: Li et al., Depletion of an immature cord blood NK subset reverses trogocytosis-driven CAR NK dysfunction, Cancer Cell (2026), https://doi.org/10.1016/j.ccell.2026.06.017

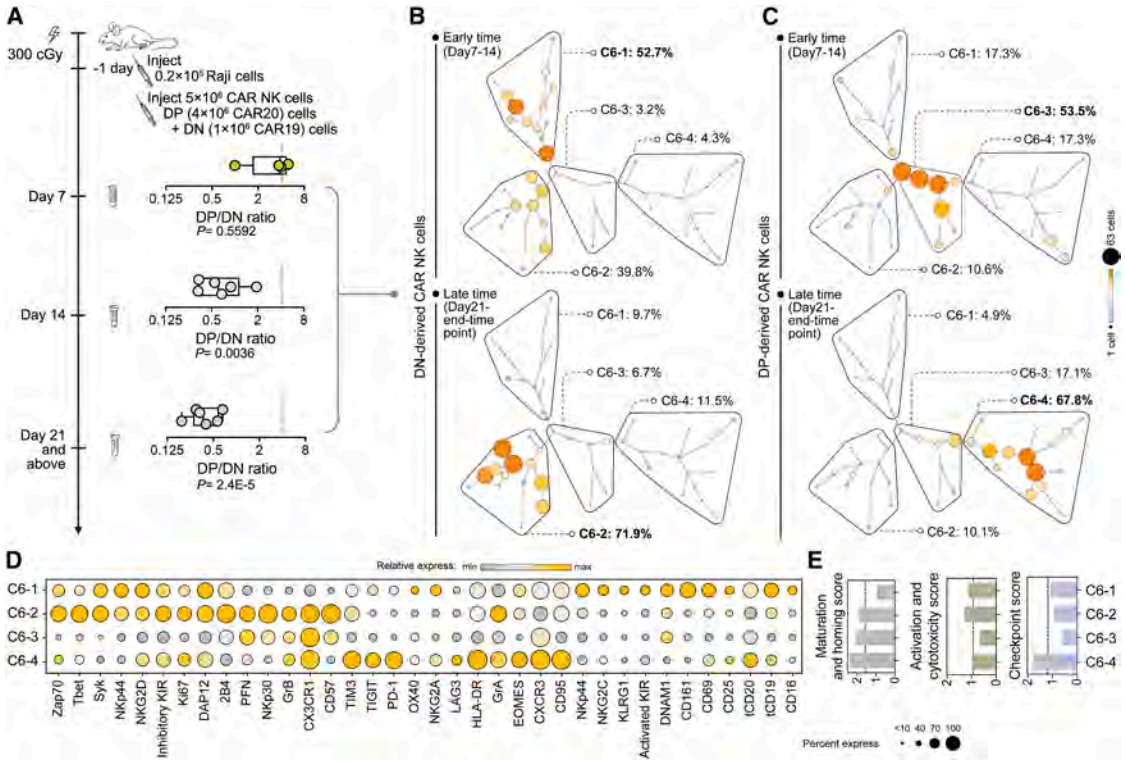

Figure 6. DN-derived NK cells impair CAR NK antitumor function and *in vivo* tumor control

(A) Schematic of the Raji lymphoma xenograft model and DP/DN ratios at the indicated time points. NSG mice received a single infusion of CAR NK cells derived from DN and/or DP CB-NK cell subsets. To enable *in vivo* tracking, DN-derived NK cells were transduced with CAR19/IL-15 and DP-derived NK cells with CAR20/IL-15 (n = 6 mice per group). Organs (spleen and bone marrow) were collected at multiple time points to monitor infused CAR NK cells over time that homed to tumor bed. p values were determined using two-tailed paired Student's t test.

(B and C) CyTOF phenotypic profiling of CAR NK cells recovered from the bone marrow (BM) and spleen of treated mice (n = 6 per group per time point). Cells from (B) DN subsets and (C) DP subsets were pooled to two groups based on collection time: early time points (day 7–14) and late time points (day 21 till end-time points of treated mice). Frequencies of clusters are shown.

(D) Heatmap of marker expression across each cluster of infused CAR NK cells.

(E) Corresponding functional scores for NK cell maturation and homing, activation and cytotoxicity, and checkpoint expression. Scores were calculated from normalized marker intensities. The dashed gray line indicates the median score across the dataset.

High TROG-antigen burden drives fratricide and exhaustion of DP-derived CAR NK cells *in vivo*

To define how trogocytic antigen acquisition shapes CAR NK cell fate *in vivo*, we performed CyTOF analyses on CAR NK cells recovered from tumor-bearing organs at serial time points during tumor progression (Figure 6A; Figure S12). Consistent with PB tracking, DN-derived CAR NK cells progressively accumulated and became the dominant circulating and tissue-infiltrating resident population before relapse (Figure 6A). Early after infusion (days 7–14), DN-derived cells localized primarily to cluster C6-1 (52.7%), characterized by low maturation and activation scores. At later time points, they transitioned toward cluster C6-2 (71.9%), with increased expression of membrane proximal signaling adaptors (Zap70, Syk, DAP12, and 2B4) and cytotoxic molecules, such as GrB, granzyme A (GrA), and PFN, without high co-expression of checkpoint receptors. Notably, emergence of this state coincided with tumor relapse (Figures 6B–6E; Figures S11F–S11J), suggesting limited productive CAR-driven tumor control despite partial acquisition of effector features. In contrast, DP-derived CAR NK cells initially populated clusters C6-3 (53.5%) and later C6-4 (67.8%; Figure 6C). These cells maintained higher scores for maturation and homing and expressed activation-associated markers including DAP12, CD69, HLA-DR, and CX3CR1. Over time, however, DP-derived CAR NK cells showed progressive loss of CD16, CD161, and key adaptor molecules (Zap70, Syk, and 2B4; Figure 6D). By late stages, C6-4 cells displayed an increased EOMES to T-bet ratio with persistently high Fas expression that could trigger FADD-mediated cell apoptosis[35,36] and the co-expression of TIGIT, TIM3, PD-1, and LAG3, consistent with transition toward functional exhaustion *in vivo*.[10]

We next asked whether this deterioration in DP-derived effector state was linked to TROG-antigen accumulation and to the presence of DN-derived cells in the infused product. We compared phenotypes in mice receiving DN-only, DP-only, or mixed DP plus DN products (Figures S13 and S14). DN-derived CAR NK cells accumulated high levels of TROG-antigen whether infused alone or in mixtures, and their phenotypic trajectory was largely unchanged (Figures S13A and S14A). In contrast, DP-derived CAR NK cells infused alone showed low TROG-antigen

Please cite this article in press as: Li et al., Depletion of an immature cord blood NK subset reverses trogocytosis-driven CAR NK dysfunction, Cancer Cell (2026), https://doi.org/10.1016/j.ccell.2026.06.017

CellPress
OPEN ACCESS

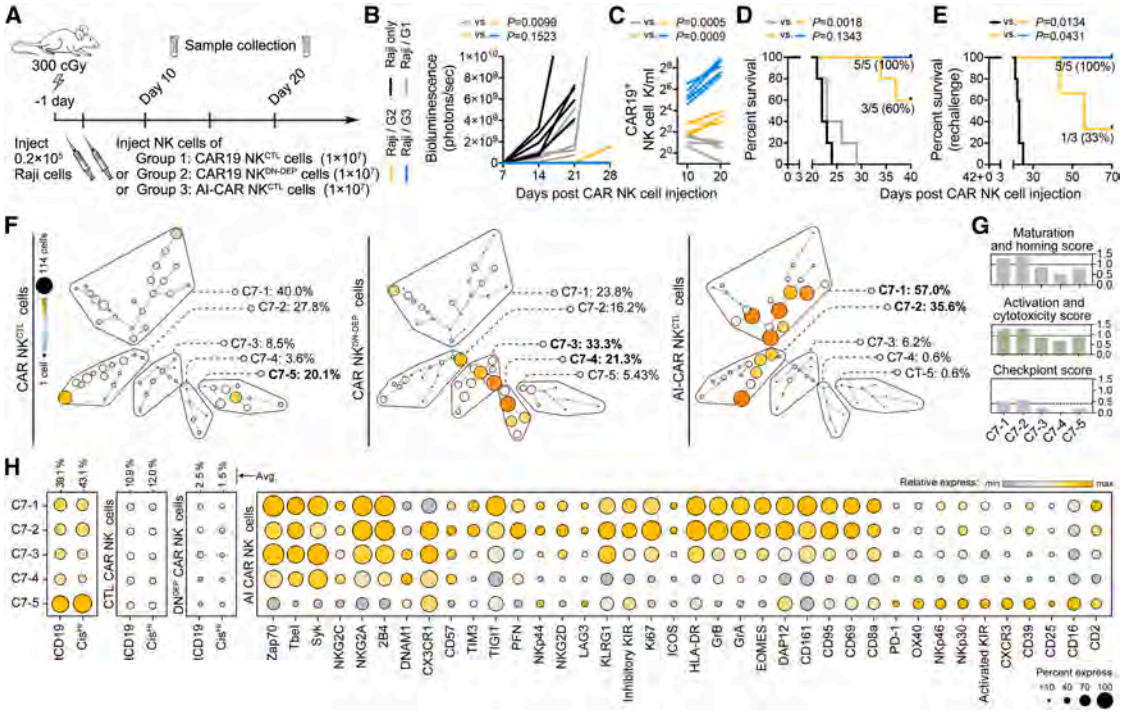

Figure 7. Depletion of DN cells from donor CB-NK cells restores CAR NK cell-mediated antitumor activity *in vivo*

(A) Raji xenograft study design. Mice received a single infusion of 1×10^7 CAR19/IL-15 NK cells, manufactured either from CB donors depleted of the DN subset before *ex vivo* expansion and CAR engineering (DN-DEP; group 2, G2) or from mock-sorted donors without subset depletion (group 1, G1). A third group received CAR19/IL-15 NK cells co-expressing an inhibitory CAR targeting the NK self-antigen CS1 (AI-CAR, CAR19+iCAR; group 3, G3). Tumor-only mice served as untreated controls (n = 5 mice per group).

(B) Tumor burden monitored weekly by bioluminescence imaging (BLI) and presented as normalized BLI intensity. Each line represents an individual mouse.

(C) Quantification of viable CAR19/IL-15 NK cells in peripheral blood (PB) over time. Each line represents an individual mouse.

(D and E) Kaplan-Meier survival curves after (D) initial Raji challenge and (E) and after Raji rechallenge on day 42.

(F) CyTOF profiling of CAR NK cells early post-infusion (n = 5 mice per group); cluster frequencies are indicated.

(G) Functional scores across 5 post-infusion CAR NK cell clusters. Dashed gray lines indicate dataset medians.

(H) Heatmap showing marker expression across post-infusion clusters. Data were pooled from 5 mice per group.

p values were calculated by two-tailed two-way ANOVA (B and C) and log rank test (D and E). Data were assessed through flow cytometry (C) or CyTOF (F–H).

expression and better viability and maintained a robust effector profile (Figure S13B). At single-cell level resolution, DP-derived CAR NK cells were enriched in clusters DP-1 to DP-3 (80.9% in total), marked by high expression of NKRs and NCRs, CD16, CD161, KLRG1, co-activation markers (CD8a, CD69, and HLA-DR), EOMES, T-bet, and cytotoxic molecules, consistent with a mature, activated, and cytotoxic state (Figures S14B–S14E). Strikingly, when co-infused with DN-derived cells, DP CAR NK cells shifted away from DP-1 to DP-3 and accumulated instead in DP-5 (40.6%) and DP-6 (44.5%). These clusters were characterized by markedly higher TROG-antigen levels, reduced viability, and downregulation of key NK receptors (Figures S14B–S14E). Although DP-5 and DP-6 cells retained partial cytotoxic potential and trafficking features, they expressed high Fas and HLA-DR, and DP-5 showed prominent co-expression of multiple checkpoint molecules, consistent with sustained activation followed by exhaustion (Figures S14B–S14E). Tumor relapse occurred early in these mixed product groups.

Together, these data support an *in vivo* model in which DN-derived CAR NK cells, despite limited intrinsic tumor control, contribute to high TROG-antigen accumulation that redistributes cognate antigen within the effector compartment. This, in turn, promotes fratricide and prolonged CAR engagement, accelerating activation-induced attrition and exhaustion of DP-derived CAR NK cells and thereby undermining durable tumor control.

Depleting the DN subset restores CB-CAR NK cell antitumor activity *in vivo*

Our results suggested that immature DN-NK cells limit the antitumor efficacy of CB-derived CAR NK cell products, particularly in donors with low DP-to-DN ratios. We therefore asked whether physical depletion of DN cells could restore antitumor function *in vivo*. Using an NSG Raji lymphoma model, we generated CAR19/IL-15 NK cells from 4 CB donors with low DP/DN ratios (median, 4.3; range, 3.0–5.2). For each donor, matched CAR NK cell products were manufactured either after depletion (DEP) of $CD16^-CD161^-$ DN cells (CAR NK^{DN-DEP}) or after mock-sorting as a control (CAR NK^{CTL}; Figure 7A). Because TROG-antigen accumulation and effector fratricide emerged as key mechanisms of failure in DN-containing products, we also included a control in which mock-sorted cells were engineered with both an activating anti-CD19 CAR and an inhibitory CAR

Please cite this article in press as: Li et al., Depletion of an immature cord blood NK subset reverses trogocytosis-driven CAR NK dysfunction, Cancer Cell (2026), https://doi.org/10.1016/j.ccell.2026.06.017

recognizing the NK-cell-specific self-antigen CS1, termed (AI-CAR NK^{CTL}). In this configuration, the anti-CD19 CAR directs tumor killing while CS1 engagement on neighboring NK cells delivers an inhibitory signal that protects TROG-positive CAR NK cells from NK-to-NK cell fratricide. Thus, the AI-CAR design preserves antitumor cytotoxicity while limiting TROG-antigen transfer-driven cytotoxicity.[10]

DN depletion significantly improved *in vivo* antitumor activity. Mice treated with CAR19 NK^{DN-DEP} cells showed lower bioluminescence imaging (BLI) tumor burden, improved CAR NK cell persistence, and better survival than mice treated with CAR19 NK^{CTL} cells, which showed limited persistence and poor tumor control (Figures 7B–7D; Figure S15A). After the second tumor rechallenge, CAR19 NK^{DN-DEP} cells also achieved durable complete remission in one of three mice, sustained for up to 360 days, while AI-CAR NK^{CTL} cells produced the strongest overall activity, with complete remission in all treated mice (Figure 7E; Figure S15B), consistent with protection from fratricide and improved *in vivo* persistence.

CyTOF profiling of infused products and after early recovery from treated mice supported these functional findings. CAR NK^{CTL} cells, but not cells of their non-CAR expressing NK compartment, showed substantial TROG-antigen accumulation (39.1%) and reduced viability (56.9%; Figures 7F–7H; Figures S15C and S15D). In contrast, both CAR NK^{DN-DEP} and AI-CAR NK^{CTL} cell products had lower TROG-antigen burden, improved viability, and reduced representation of the dysfunctional C7-5 cluster, which was characterized by low expression of NK cell functional receptors, signaling adaptors, and cytotoxic molecules (Figures 7F–7H). CAR NK^{DN-DEP} cells and AI-CAR NK^{CTL} cells expressed similar levels of membrane-proximal signaling adaptors, including Zap70, Syk, and 2B4. However, CAR NK^{DN-DEP} cells retained a sizable (54.6%) population in C7-3 and C7-4, with lower PFN, GrB, and GrA; reduced activation markers (e.g., TIM3, HLA-DR, DAP12, and CD69); and low Fas expression (Figures 7F–7H). In contrast, AI-CAR NK^{CTL} cells were predominantly enriched in C7-1 and C7-2 (92.6% in total), clusters characterized by high Ki67 expression, increased maturation, homing capacity, activation, and cytotoxic potential, with limited checkpoint expression (Figures 7F–7H). Together, these data show that DN depletion improves CB-CAR NK cell potency *in vivo*, while AI-CAR engineering provides additional protection that further supports persistence and tumor control.

We next asked whether DN depletion improved activity in a solid tumor setting. In an intraperitoneal SKOV3 ovarian cancer model with endogenous TROP2 expression, mice received CAR.TROP2/IL-15 NK cells generated from the same CB donor either with DN subset depletion before expansion and CAR engineering or without subset depletion. As an additional control, mice received AI-CAR NK cells manufactured from the same CB-NK donor without DN depletion (Figure S16). As in the Raji model, CAR NK^{DN-DEP}- and AI-CAR NK^{CTL}-treated groups showed improved tumor control, greater *in vivo* persistence, and improved overall survival compared with CAR NK^{CTL} cells (Figures S16C–S16E).

Together, these results demonstrate that removal of the DN subset from CB-NK cells restores *in vivo* CAR NK cell antitumor activity by reducing TROG-antigen burden, thereby diminishing TAS-driven fratricide and activation-induced attrition. This simple manufacturing intervention preserves CAR NK cell persistence and effector functionality, with the largest gain in donors whose starting NK cell compartment is enriched for DN cells.

DISCUSSION

CAR NK cell-based therapy is an attractive platform for adoptive immunotherapy because it can be manufactured from available donor sources,[8,42,43] has a favorable safety profile, and leverages multiple cytotoxic mechanisms.[4,7,8] Yet, clinical translation remains limited by donor-to-donor variability and inconsistent persistence and tumor control after engineering.[8]

Here, we identify an immature NK cell subset in CB as a major determinant of CAR NK cell product performance. NK cells that lack both CD16 and CD161 (DN-NK cells) in unexpanded CB units produced CAR NK effectors with limited tumor responsiveness and critically impaired the activity of otherwise potent effectors derived from the $CD16^+CD161^+$ DP subset. Integrated single-cell transcriptomic and protein profiling linked subset of origin with divergent effector programs after expansion. DP-derived NK cells retained coordinated expression of natural cytotoxicity receptors, membrane-proximal signaling adaptors, and cytotoxic effector modules consistent with effective cell-to-cell killing. In contrast, DN-derived NK cells preserved an innate response architecture enriched for cytokine responsiveness and endosomal-sensing pathways, with only partial acquisition of maturation markers after expansion. Functionally, DN-derived CAR NK cells remained hyporesponsive to antigen challenge, whereas DP-derived CAR NK cells mediated strong tumor control but showed greater susceptibility to activation-induced attrition under sustained engagement.

A central mechanistic insight is that DN-derived CAR NK cells reshape the effector population through disproportionate trogocytic acquisition of cognate antigen. After tumor encounter, DN-derived CAR NK cells accumulated higher levels of surface cognate antigen, consistent with antigen stripping from tumors that was uncoupled from efficient target cell lysis. We propose that this creates a TAS, in which transferred tumor antigen accumulates on CAR NK cells and creates competing on-target cognate ligands within the effector pool. TAS formation creates competing on-target ligands within the effector pool, diverting CAR engagement away from tumor cells and onto TROG-antigen positive sibling effectors. This redirects the most cytotoxic DP-derived CAR NK cells into fratricidal interactions, accelerating AICD and promoting an exhaustion-associated phenotype. This model is supported by multiple orthogonal experimental systems, including single-cell killing analyses, mixed DN/DP spheroid coculture assays, and *in vivo* tracking data, where DN-containing products showed early loss of DP effectors, persistence of DN-derived cells and failure to sustain tumor control. These findings have immediate implications for donor selection and manufacturing. CB units enriched for DN cells represent a suboptimal starting material, whereas products enriched for $CD16^+CD161^+$ DP mature subset are associated with improved functional output.[8] Consistent with this, depletion of the DN subset before CAR NK cell manufacturing restored efficacy in both lymphoma and solid tumor models, improving tumor control and persistence similar to logic-gated activating/inhibitory CAR configuration that limits self-recognition-driven fratricide.[10,44]

In summary, we define DN subset content as a major driver of CAR NK cell product failure and establish TAS-mediated antigen redistribution as a population level mechanism that links TROG to fratricide, DP depletion, and loss of efficacy. DN depletion provides a practical and scalable intervention to improve product consistency. More broadly, strategies that limit TAS formation, either through starting material composition or CAR circuit design, may further enhance potency, persistence, and therapeutic efficacy of CAR NK cells.

RESOURCE AVAILABILITY

Lead contact

Further information and requests for resources and reagents should be directed to and will be fulfilled by the lead contact, Katayoun Rezvani (krezvani@mdanderson.org).

Materials availability

All requests for data and materials will be reviewed by MD Anderson Cancer Center to verify whether the request is subject to any intellectual property of confidentiality obligations. Any data and materials that can be shared by the corresponding authors will be released freely or via a materials transfer agreement, if deemed necessary.

Data and code availability

- Transcriptome data derived from GEM-flex single-cell sequencing used in the generation of Figures 2 and 3 are available through the Gene Expression Omnibus (https://www.ncbi.nlm.nih.gov/geo/) under accession number GSE313836.
- No custom code was developed for this research article.

ACKNOWLEDGMENTS

This work was supported in part by the generous philanthropic contributions to The University of Texas MD Anderson Cancer Center Institute for Cell Therapy Discovery and Innovation, including lead commitments from Meg and Kirk Gentle, the Lindonlight Collective, The Marcus Foundation, Inc., the Margery L. Block Foundation, theMelville Foundation, and the Tanoto Foundation; additional significant support from the James B. and Lois R. Archer Charitable Foundation, Ann and Clarence Cazalot, the Cockrell Foundation, the Cyvia & Melvyn Wolff Family Foundation, Vijay and Marie Goradia, Melvyn N. Klein, the Marek Family Foundation, Gayle Stoffel, the McCombs Foundation, the Walters Family, and MD Anderson's Accelerator Fund; the Sally Cooper Murray endowment; grants (grant nos. 1 R01 CA211044–01, 5 P01CA148600–03, and R01CA288617-01) from the National Institutes of Health (NIH); and the Specialized Program of Research Excellence (SPORE) grants in Ovarian Cancer (5P50CA281701–02) and Leukemia (P50CA100632). The MD Anderson Cancer Center Advanced Technology Genomics Core (ATGC) Facility was supported in part by a grant from the NIH (grant nos. CA016672 and 1S10OD024977–01). The Flow Cytometry and Cellular Imaging Core Facility was supported in part by The University of Texas MD Anderson Cancer Center, P30CA016672. Diagrams were prepared in BioRender. com.

AUTHOR CONTRIBUTIONS

Y.L. and K.R. conducted conceptualization of the study, completed the experimental design, and interpreted and analyzed the data; Y.L. directed *in vitro* and *in vivo* experiments with assistance from G.W. and X.W.; Y.L. and H.F. planned and performed the experiments and analyzed the scRNA-seq data with assistance from P.Z.; Y.L. and M.N.M. planned and performed metabolic analyses; Y.L., R.B., N.U., and R.S. prepared and performed mass cytometry experiments and analyses; N.W.F. performed pathologic evaluation of *in vivo* work; Y.L. and B.L. designed and prepared CAR vector; Y.L., L.L.P., P.M., E.D., and N.V. executed single-cell imaging and analysis; J.W. collected and prepared frozen CBUs; Y.L. drafted original writing; M.D, E.D., N.V., and E.J.S. commented on the manuscript, which was reviewed and edited by Y.L., G.M.D., L.M.F., and K.R.

DECLARATION OF INTERESTS

Y.L., R.B., N.U., E.L., P.P.B., M.D., D.M., E.J.S, K.R., and The University of Texas MD Anderson Cancer Center have an institutional financial conflict of interest with Takeda Pharmaceuticals. R.B., E.L., E.J.S., K.R., and The University of Texas MD Anderson Cancer Center have an institutional financial conflict of interest with Affimed. N.V. is a co-founder of CellChorus and AuraVax. K.R. participates on the scientific advisory board for Avenge Bio, Virogin Biotech, Navan Technologies, Caribou Biosciences, Bit Bio Limited, Replay Holdings, oNKo Innate, the Alliance for Cancer Gene Therapy ACGT, Innate Pharma, and Shinobi Therapeutics. K.R. is the scientific founder of Syena. M.D. participates on the scientific advisory board of Cellsbin, Aurigene, and Bruker Cellular Analysis. E.J.S. participates on the scientific advisory board for Adaptimmune Limited, Axio Research, Celaid Therapeutics, FibroBiologics, Navan Technologies, New York Blood Center, and Zelluna. P.P.B. participates on the scientific advisory board for Dialectica.

STAR★METHODS

Detailed methods are provided in the online version of this paper and include the following:

- KEY RESOURCES TABLE
- EXPERIMENTAL MODEL AND STUDY PARTICIPANT DETAILS
  - Cell lines, primary cells, and culture conditions
  - Manufacture of CAR NK cells from CBUs
- METHOD DETAILS
  - Cell preparation for single-cell RNA sequencing
  - Single-cell library preparation for GEX and ADT
  - 10× genomics chromium 3′ scRNA-seq data preprocessing and analysis for CB-NK cell
  - Preprocessing of single cell GEX and ADT data for expanded NK cell subsets
  - DN/DP-specific and -unique signatures
  - CAR NK cell population doubling assay
  - IsoPlexis assay
  - IFN-γ secretion assay
  - Flow cytometry
  - Metabolism assays
  - Tumor rechallenge assay in IncuCyte system
  - Spheroid killing assay and TAS evaluation
  - Single-cell cytotoxicity assay
  - Mass cytometry (CyTOF)
  - Mass cytometry data analysis
  - Xenogeneic tumor-grafted mouse models
- QUANTIFICATION AND STATISTICAL ANALYSIS
  - Statistics

SUPPLEMENTAL INFORMATION

Supplemental information can be found online at https://doi.org/10.1016/j.ccell.2026.06.017.

Received: January 26, 2026
Revised: May 26, 2026
Accepted: June 25, 2026

REFERENCES

1. Hamieh, M., Mansilla-Soto, J., Rivière, I., and Sadelain, M. (2023). Programming CAR T Cell Tumor Recognition: Tuned Antigen Sensing and Logic Gating. Cancer Discov. *13*, 829–843. https://doi.org/10.1158/2159-8290.CD-23-0101.

2. Zugasti, I., Espinosa-Aroca, L., Fidyt, K., Mulens-Arias, V., Diaz-Beya, M., Juan, M., Urbano-Ispizua, Á., Esteve, J., Velasco-Hernandez, T., and Menéndez, P. (2025). CAR-T cell therapy for cancer: current challenges and future directions. Signal Transduct. Targeted Ther. *10*, 210. https://doi.org/10.1038/s41392-025-02269-w.

3. Baker, D.J., Arany, Z., Baur, J.A., Epstein, J.A., and June, C.H. (2023). CAR T therapy beyond cancer: the evolution of a living drug. Nature *619*, 707–715. https://doi.org/10.1038/s41586-023-06243-w.

4. Biederstädt, A., and Rezvani, K. (2025). Engineered natural killer cells for cancer therapy. Cancer Cell *43*, 1987–2013. https://doi.org/10.1016/j.ccell.2025.09.013.

5. Vivier, E., Rebuffet, L., Narni-Mancinelli, E., Cornen, S., Igarashi, R.Y., and Fantin, V.R. (2024). Natural killer cell therapies. Nature *626*, 727–736. https://doi.org/10.1038/s41586-023-06945-1.

6. Myers, J.A., and Miller, J.S. (2021). Exploring the NK cell platform for cancer immunotherapy. Nat. Rev. Clin. Oncol. *18*, 85–100. https://doi.org/10.1038/s41571-020-0426-7.

7. Chen, S., Zhu, H., and Jounaidi, Y. (2024). Comprehensive snapshots of natural killer cells functions, signaling, molecular mechanisms and clinical utilization. Signal Transduct. Targeted Ther. *9*, 302. https://doi.org/10.1038/s41392-024-02005-w.

8. Marin, D., Li, Y., Basar, R., Rafei, H., Daher, M., Dou, J., Mohanty, V., Dede, M., Nieto, Y., Uprety, N., et al. (2024). Safety, efficacy and determinants of response of allogeneic CD19-specific CAR-NK cells in CD19(+) B cell tumors: a phase 1/2 trial. Nat. Med. *30*, 772–784. https://doi.org/10.1038/s41591-023-02785-8.

9. Liu, E., Marin, D., Banerjee, P., Macapinlac, H.A., Thompson, P., Basar, R., Nassif Kerbauy, L., Overman, B., Thall, P., Kaplan, M., et al. (2020). Use of CAR-Transduced Natural Killer Cells in CD19-Positive Lymphoid Tumors. N. Engl. J. Med. *382*, 545–553. https://doi.org/10.1056/NEJMoa1910607.

10. Li, Y., Basar, R., Wang, G., Liu, E., Moyes, J.S., Li, L., Kerbauy, L.N., Uprety, N., Fathi, M., Rezvan, A., et al. (2022). KIR-based inhibitory CARs overcome CAR-NK cell trogocytosis-mediated fratricide and tumor escape. Nat. Med. *28*, 2133–2144. https://doi.org/10.1038/s41591-022-02003-x.

11. Hamieh, M., Dobrin, A., Cabriolu, A., van der Stegen, S.J.C., Giavridis, T., Mansilla-Soto, J., Eyquem, J., Zhao, Z., Whitlock, B.M., Miele, M.M., et al. (2019). CAR T cell trogocytosis and cooperative killing regulate tumour antigen escape. Nature *568*, 112–116. https://doi.org/10.1038/s41586-019-1054-1.

12. Romee, R., Foley, B., Lenvik, T., Wang, Y., Zhang, B., Ankarlo, D., Luo, X., Cooley, S., Verneris, M., Walcheck, B., and Miller, J. (2013). NK cell CD16 surface expression and function is regulated by a disintegrin and metalloprotease-17 (ADAM17). Blood *121*, 3599–3608. https://doi.org/10.1182/blood-2012-04-425397.

13. Poli, A., Michel, T., Thérésine, M., Andrès, E., Hentges, F., and Zimmer, J. (2009). CD56bright natural killer (NK) cells: an important NK cell subset. Immunology *126*, 458–465. https://doi.org/10.1111/j.1365-2567.2008.03027.x.

14. Dalle, J.H., Menezes, J., Wagner, E., Blagdon, M., Champagne, J., Champagne, M.A., and Duval, M. (2005). Characterization of cord blood natural killer cells: implications for transplantation and neonatal infections. Pediatr. Res. *57*, 649–655. https://doi.org/10.1203/01.PDR.0000156501.55431.20.

15. Wyrożemski, Ł., and Qiao, S.W. (2021). Immunobiology and conflicting roles of the human CD161 receptor in T cells. Scand. J. Immunol. *94*, e13090. https://doi.org/10.1111/sji.13090.

16. Kurioka, A., Cosgrove, C., Simoni, Y., van Wilgenburg, B., Geremia, A., Björkander, S., Sverremark-Ekström, E., Thurnheer, C., Günthard, H.F., Khanna, N., et al. (2018). CD161 Defines a Functionally Distinct Subset of Pro-Inflammatory Natural Killer Cells. Front. Immunol. *9*, 486. https://doi.org/10.3389/fimmu.2018.00486.

17. Abe, S., Kagao, M., Asahi, T., Kato, R., Tani-Ichi, S., Shimba, A., Ishibashi, R., Miyachi, H., Kitano, S., Miyazaki, M., et al. (2025). The transcription factor RORalpha is required for the development of type 1 innate lymphoid cells in adult bone marrow. J. Immunol. *214*, 575–581. https://doi.org/10.1093/jimmun/vkaf001.

18. Wang, R., Campbell, S., Amir, M., Mosure, S.A., Bassette, M.A., Eliason, A., Sundrud, M.S., Kamenecka, T.M., and Solt, L.A. (2021). Genetic and pharmacological inhibition of the nuclear receptor RORalpha regulates T(H)17 driven inflammatory disorders. Nat. Commun. *12*, 76. https://doi.org/10.1038/s41467-020-20385-9.

19. Wong, W.F., Kohu, K., Chiba, T., Sato, T., and Satake, M. (2011). Interplay of transcription factors in T-cell differentiation and function: the role of Runx. Immunology *132*, 157–164. https://doi.org/10.1111/j.1365-2567.2010.03381.x.

20. Kirk, S.G., Samavati, L., and Liu, Y. (2020). MAP kinase phosphatase-1, a gatekeeper of the acute innate immune response. Life Sci. *241*, 117157. https://doi.org/10.1016/j.lfs.2019.117157.

21. Soares-Silva, M., Diniz, F.F., Gomes, G.N., and Bahia, D. (2016). The Mitogen-Activated Protein Kinase (MAPK) Pathway: Role in Immune Evasion by Trypanosomatids. Front. Microbiol. *7*, 183. https://doi.org/10.3389/fmicb.2016.00183.

22. Ferré, C.A., Thouard, A., Bétourné, A., Le Dorze, A.L., Belenguer, P., Miquel, M.C., Peyrin, J.M., Gonzalez-Dunia, D., and Szelechowski, M. (2021). HSPA9/Mortalin mediates axo-protection and modulates mitochondrial dynamics in neurons. Sci. Rep. *11*, 17705. https://doi.org/10.1038/s41598-021-97162-1.

23. Qian, S., Wei, Z., Yang, W., Huang, J., Yang, Y., and Wang, J. (2022). The role of BCL-2 family proteins in regulating apoptosis and cancer therapy. Front. Oncol. *12*, 985363. https://doi.org/10.3389/fonc.2022.985363.

24. Vogler, M., Braun, Y., Smith, V.M., Westhoff, M.A., Pereira, R.S., Pieper, N.M., Anders, M., Callens, M., Vervliet, T., Abbas, M., et al. (2025). The BCL2 family: from apoptosis mechanisms to new advances in targeted therapy. Signal Transduct. Targeted Ther. *10*, 91. https://doi.org/10.1038/s41392-025-02176-0.

25. Guo, Q., Jin, Y., Chen, X., Ye, X., Shen, X., Lin, M., Zeng, C., Zhou, T., and Zhang, J. (2024). NF-kappaB in biology and targeted therapy: new insights and translational implications. Signal Transduct. Targeted Ther. *9*, 53. https://doi.org/10.1038/s41392-024-01757-9.

26. Tummers, B., Mari, L., Guy, C.S., Heckmann, B.L., Rodriguez, D.A., Rühl, S., Moretti, J., Crawford, J.C., Fitzgerald, P., Kanneganti, T.D., et al. (2020). Caspase-8-Dependent Inflammatory Responses Are Controlled by Its Adaptor, FADD, and Necroptosis. Immunity *52*, 994–1006.e8. https://doi.org/10.1016/j.immuni.2020.04.010.

27. Michallet, M.C., Meylan, E., Ermolaeva, M.A., Vazquez, J., Rebsamen, M., Curran, J., Poeck, H., Bscheider, M., Hartmann, G., König, M., et al. (2008). TRADD protein is an essential component of the RIG-like helicase antiviral pathway. Immunity *28*, 651–661. https://doi.org/10.1016/j.immuni.2008.03.013.

28. Björkström, N.K., Strunz, B., and Ljunggren, H.G. (2022). Natural killer cells in antiviral immunity. Nat. Rev. Immunol. *22*, 112–123. https://doi.org/10.1038/s41577-021-00558-3.

29. Adib-Conquy, M., Scott-Algara, D., Cavaillon, J.M., and Souza-Fonseca-Guimaraes, F. (2014). TLR-mediated activation of NK cells and their role in bacterial/viral immune responses in mammals. Immunol. Cell Biol. *92*, 256–262. https://doi.org/10.1038/icb.2013.99.

30. Noh, J.Y., Yoon, S.R., Kim, T.D., Choi, I., and Jung, H. (2020). Toll-Like Receptors in Natural Killer Cells and Their Application for Immunotherapy. J. Immunol. Res. *2020*, 2045860. https://doi.org/10.1155/2020/2045860.

31. Lauzon, N.M., Mian, F., MacKenzie, R., and Ashkar, A.A. (2006). The direct effects of Toll-like receptor ligands on human NK cell cytokine production and cytotoxicity. Cell. Immunol. *241*, 102–112. https://doi.org/10.1016/j.cellimm.2006.08.004.

32. Bertheloot, D., Latz, E., and Franklin, B.S. (2021). Necroptosis, pyroptosis and apoptosis: an intricate game of cell death. Cell. Mol. Immunol. *18*, 1106–1121. https://doi.org/10.1038/s41423-020-00630-3.

33. Arakaki, R., Yamada, A., Kudo, Y., Hayashi, Y., and Ishimaru, N. (2014). Mechanism of activation-induced cell death of T cells and regulation of FasL expression. Crit. Rev. Immunol. *34*, 301–314. https://doi.org/10.1615/critrevimmunol.2014009988.

34. Varadhachary, A.S., Perdow, S.N., Hu, C., Ramanarayanan, M., and Salgame, P. (1997). Differential ability of T cell subsets to undergo activation-induced cell death. Proc. Natl. Acad. Sci. USA *94*, 5778–5783. https://doi.org/10.1073/pnas.94.11.5778.

35. Yi, F., Cohen, T., Zimmerman, N., Dündar, F., Zumbo, P., Eltilib, R., Brophy, E.J., Arkin, H., Feucht, J., Gormally, M.V., et al. (2025). CAR-engineered lymphocyte persistence is governed by a FAS ligand-FAS autoregulatory circuit. Nat. Cancer *6*, 1638–1655. https://doi.org/10.1038/s43018-025-01009-x.

36. Osborn, S.L., Diehl, G., Han, S.J., Xue, L., Kurd, N., Hsieh, K., Cado, D., Robey, E.A., and Winoto, A. (2010). Fas-associated death domain (FADD) is a negative regulator of T-cell receptor-mediated necroptosis. Proc. Natl. Acad. Sci. USA *107*, 13034–13039. https://doi.org/10.1073/pnas.1005997107.

37. Sikora, E. (2015). Activation-induced and damage-induced cell death in aging human T cells. Mech. Ageing Dev. *151*, 85–92. https://doi.org/10.1016/j.mad.2015.03.011.

38. Miao, E.A., Rajan, J.V., and Aderem, A. (2011). Caspase-1-induced pyroptotic cell death. Immunol. Rev. *243*, 206–214. https://doi.org/10.1111/j.1600-065X.2011.01044.x.

39. Delgoffe, G.M., Xu, C., Mackall, C.L., Green, M.R., Gottschalk, S., Speiser, D.E., Zehn, D., and Beavis, P.A. (2021). The role of exhaustion in CAR T cell therapy. Cancer Cell *39*, 885–888. https://doi.org/10.1016/j.ccell.2021.06.012.

40. Selli, M.E., Landmann, J.H., Arveseth, C., and Singh, N. (2023). Inducing T cell dysfunction by chronic stimulation of CAR-engineered T cells targeting cancer cells in suspension cultures. STAR Protoc. *4*, 101954. https://doi.org/10.1016/j.xpro.2022.101954.

41. Huan, T., Chen, D., Liu, G., Zhang, H., Wang, X., Wu, Z., Wu, Y., Xu, Q., and Yu, F. (2022). Activation-induced cell death in CAR-T cell therapy. Hum. Cell *35*, 441–447. https://doi.org/10.1007/s13577-022-00670-z.

42. Li, Y., Hermanson, D.L., Moriarity, B.S., and Kaufman, D.S. (2018). Human iPSC-Derived Natural Killer Cells Engineered with Chimeric Antigen Receptors Enhance Anti-tumor Activity. Cell Stem Cell *23*, 181–192.e5. https://doi.org/10.1016/j.stem.2018.06.002.

43. Zhang, B., Yang, M., Zhang, W., Liu, N., Wang, D., Jing, L., Xu, N., Yang, N., and Ren, T. (2024). Chimeric antigen receptor-based natural killer cell immunotherapy in cancer: from bench to bedside. Cell Death Dis. *15*, 50. https://doi.org/10.1038/s41419-024-06438-7.

44. Li, Y., Rezvani, K., and Rafei, H. (2023). Next-generation chimeric antigen receptors for T- and natural killer-cell therapies against cancer. Immunol. Rev. *320*, 217–235. https://doi.org/10.1111/imr.13255.

45. Lander, E.S., Linton, L.M., Birren, B., Nusbaum, C., Zody, M.C., Baldwin, J., Devon, K., Dewar, K., Doyle, M., FitzHugh, W., et al. (2001). Initial sequencing and analysis of the human genome. Nature *409*, 860–921. https://doi.org/10.1038/35057062.

46. Schneider, V.A., Graves-Lindsay, T., Howe, K., Bouk, N., Chen, H.C., Kitts, P.A., Murphy, T.D., Pruitt, K.D., Thibaud-Nissen, F., Albracht, D., et al. (2017). Evaluation of GRCh38 and de novo haploid genome assemblies demonstrates the enduring quality of the reference assembly. Genome Res. *27*, 849–864. https://doi.org/10.1101/gr.213611.116.

47. Zheng, G.X.Y., Terry, J.M., Belgrader, P., Ryvkin, P., Bent, Z.W., Wilson, R., Ziraldo, S.B., Wheeler, T.D., McDermott, G.P., Zhu, J., et al. (2017). Massively parallel digital transcriptional profiling of single cells. Nat. Commun. *8*, 14049. https://doi.org/10.1038/ncomms14049.

48. Stuart, T., Butler, A., Hoffman, P., Hafemeister, C., Papalexi, E., Mauck, W.M., Hao, Y., Stoeckius, M., Smibert, P., and Satija, R. (2019). Comprehensive Integration of Single-Cell Data. Cell *177*, 1888–1902.e21. https://doi.org/10.1016/j.cell.2019.05.031.

49. Germain, P.L., Lun, A., Garcia Meixide, C., Macnair, W., and Robinson, M.D. (2021). Doublet identification in single-cell sequencing data using scDblFinder. F1000Res. *10*, 979. https://doi.org/10.12688/f1000research.73600.2.

50. Yu, G., Wang, L.G., Han, Y., and He, Q.Y. (2012). clusterProfiler: an R package for comparing biological themes among gene clusters. OMICS *16*, 284–287. https://doi.org/10.1089/omi.2011.0118.

51. Street, K., Risso, D., Fletcher, R.B., Das, D., Ngai, J., Yosef, N., Purdom, E., and Dudoit, S. (2018). Slingshot: cell lineage and pseudotime inference for single-cell transcriptomics. BMC Genom. *19*, 477. https://doi.org/10.1186/s12864-018-4772-0.

52. Van den Berge, K., Roux de Bézieux, H., Street, K., Saelens, W., Cannoodt, R., Saeys, Y., Dudoit, S., and Clement, L. (2020). Trajectory-based differential expression analysis for single-cell sequencing data. Nat. Commun. *11*, 1201. https://doi.org/10.1038/s41467-020-14766-3.

53. Butler, A., Hoffman, P., Smibert, P., Papalexi, E., and Satija, R. (2018). Integrating single-cell transcriptomic data across different conditions, technologies, and species. Nat. Biotechnol. *36*, 411–420. https://doi.org/10.1038/nbt.4096.

54. Hao, Y., Hao, S., Andersen-Nissen, E., Mauck, W.M., 3rd, Zheng, S., Butler, A., Lee, M.J., Wilk, A.J., Darby, C., Zager, M., et al. (2021). Integrated analysis of multimodal single-cell data. Cell *184*, 3573–3587.e29. https://doi.org/10.1016/j.cell.2021.04.048.

55. Börner, K., Blood, P.D., Silverstein, J.C., Ruffalo, M., Satija, R., Teichmann, S.A., Pryhuber, G.J., Misra, R.S., Purkerson, J.M., Fan, J., et al. (2025). Human BioMolecular Atlas Program (HuBMAP): 3D Human Reference Atlas construction and usage. Nat. Methods *22*, 845–860. https://doi.org/10.1038/s41592-024-02563-5.

56. Korsunsky, I., Millard, N., Fan, J., Slowikowski, K., Zhang, F., Wei, K., Baglaenko, Y., Brenner, M., Loh, P.R., and Raychaudhuri, S. (2019). Fast, sensitive and accurate integration of single-cell data with Harmony. Nat. Methods *16*, 1289–1296. https://doi.org/10.1038/s41592-019-0619-0.

57. Aibar, S., González-Blas, C.B., Moerman, T., Huynh-Thu, V.A., Imrichova, H., Hulselmans, G., Rambow, F., Marine, J.C., Geurts, P., Aerts, J., et al. (2017). SCENIC: single-cell regulatory network inference and clustering. Nat. Methods *14*, 1083–1086. https://doi.org/10.1038/nmeth.4463.

58. Castanza, A.S., Recla, J.M., Eby, D., Thorvaldsdóttir, H., Bult, C.J., and Mesirov, J.P. (2023). Extending support for mouse data in the Molecular Signatures Database (MSigDB). Nat. Methods *20*, 1619–1620. https://doi.org/10.1038/s41592-023-02014-7.

59. Murphy, A.E., and Skene, N.G. (2022). A balanced measure shows superior performance of pseudobulk methods in single-cell RNA-sequencing analysis. Nat. Commun. *13*, 7851. https://doi.org/10.1038/s41467-022-35519-4.

60. Love, M.I., Huber, W., and Anders, S. (2014). Moderated estimation of fold change and dispersion for RNA-seq data with DESeq2. Genome Biol. *15*, 550. https://doi.org/10.1186/s13059-014-0550-8.

61. Liadi, I., Singh, H., Romain, G., Rey-Villamizar, N., Merouane, A., Adolacion, J.R.T., Kebriaei, P., Huls, H., Qiu, P., Roysam, B., et al. (2015). Individual Motile CD4(+) T Cells Can Participate in Efficient Multikilling through Conjugation to Multiple Tumor Cells. Cancer Immunol. Res. *3*, 473–482. https://doi.org/10.1158/2326-6066.CIR-14-0195.

62. Merouane, A., Rey-Villamizar, N., Lu, Y., Liadi, I., Romain, G., Lu, J., Singh, H., Cooper, L.J.N., Varadarajan, N., and Roysam, B. (2015). Automated profiling of individual cell-cell interactions from high-throughput time-lapse imaging microscopy in nanowell grids (TIMING). Bioinformatics *31*, 3189–3197. https://doi.org/10.1093/bioinformatics/btv355.

63. Li, L., Chen, H., Marin, D., Xi, Y., Miao, Q., Lv, J., Banerjee, P.P., Shaim, H., Daher, M., Basar, R., et al. (2019). A novel immature natural killer cell subpopulation predicts relapse after cord blood transplantation. Blood Adv. *3*, 4117–4130. https://doi.org/10.1182/bloodadvances.2019000835.

64. Daher, M., Basar, R., Gokdemir, E., Baran, N., Uprety, N., Nunez Cortes, A.K., Mendt, M., Kerbauy, L.N., Banerjee, P.P., Shanley, M., et al.

(2021). Targeting a cytokine checkpoint enhances the fitness of armored cord blood CAR-NK cells. Blood *137*, 624–636. https://doi.org/10.1182/blood.2020007748.

65. Liu, E., Tong, Y., Dotti, G., Shaim, H., Savoldo, B., Mukherjee, M., Orange, J., Wan, X., Lu, X., Reynolds, A., et al. (2018). Cord blood NK cells engineered to express IL-15 and a CD19-targeted CAR show long-term persistence and potent antitumor activity. Leukemia *32*, 520–531. https://doi.org/10.1038/leu.2017.226.

66. Alfons, A., Croux, C., and Gelper, S. (2013). Sparse Least Trimmed Squares Regression for Analyzing High-Dimensional Large Data Sets. Ann. Appl. Stat. *7*, 226–248. https://doi.org/10.1214/12-Aoas575.

Please cite this article in press as: Li et al., Depletion of an immature cord blood NK subset reverses trogocytosis-driven CAR NK dysfunction, Cancer Cell (2026), https://doi.org/10.1016/j.ccell.2026.06.017

CellPress
OPEN ACCESS

STAR★METHODS

KEY RESOURCES TABLE

REAGENT or RESOURCE	Source	IDENTIFIER
Antibody		
Recombinant human monoclonal IgG1 anti-CD19 CAR FMC63, APC	Miltenyi Biotec	Cat# 130-127-343; RRID: AB_3664308
Recombinant human monoclonal IgG1 anti-CD178, PE	Miltenyi Biotec	Cat# 130-118-087; RRID: AB_2733776
Mouse monoclonal anti-human CD16, FITC	Biolegend	Cat# 302006; RRID: AB_314206
Mouse monoclonal anti-human CD19, FITC	Biolegend	Cat# 302206; RRID: AB_314236
Recombinant human monoclonal IgG1 anti-CD161, PE	Miltenyi Biotec	Cat# 130-113-596; RRID: AB_2922140
Recombinant human monoclonal IgG1 anti-CD161, APC	Miltenyi Biotec	Cat# 130-113-590; RRID: AB_2733505
Recombinant human monoclonal IgG1 anti-Biotin, PE	Miltenyi Biotec	Cat# 130-110-951; RRID: AB_2661378
Mouse monoclonal anti-human CD56 (NCAM), Brilliant Violet 650	Biolegend	Cat# 362532; RRID: AB_2565602
Rat monoclonal anti-mouse TER-119/ Erythroid Cells, APC/Cyanine7	Biolegend	Cat# 116223; RRID: AB_2137788
Rat monoclonal anti-mouse CD45, Alexa Fluor 488	Biolegend	Cat# 103122; RRID: AB_493531
Mouse monoclonal anti-human CD16, Brilliant Violet 650	Biolegend	Cat# 302042; RRID: AB_2563801
Mouse monoclonal anti-human CD56 (NCAM), Brilliant Violet 605	Biolegend	Cat# 362534; RRID: AB_2565632
Mouse monoclonal anti-human CD56 (NCAM), Brilliant Violet 510	Biolegend	Cat# 362538; RRID: AB_2565856
Mouse monoclonal anti-human CD3, APC/ Cyanine7	Biolegend	Cat# 300318; RRID: AB_314054
Mouse monoclonal anti-human ZAP70 Phospho (Tyr319)/Syk Phospho (Tyr352), PerCP/Cyanine5.5	Biolegend	Cat# 683710; RRID: AB_2687051
Rabbit monoclonal anti-cleaved caspase-8 (Asp374) (E6H8S)	Cell signaling	Cat# 98134 S; RRID: AB_3107200
AffiniPure Donkey polyclonal Anti-Mouse IgG (H + L), Alexa Fluor 647	Jackson Immune Research	Cat# 715-605-150; RRID: AB_2340862
Annexin V Apoptosis Detection Kit with 7-AAD, FITC	Biolegend	Cat# 640922
Recombinant human monoclonal IgG1 anti-biotin, APC	Miltenyi Biotec	Cat# 130-110-952; RRID: AB_2661378
Mouse monoclonal anti-human CD15, PE	BD Bioscience	Cat# 555402; RRID: AB_395802
Mouse monoclonal anti-human CD14, PE	BD Bioscience	Cat# 555398; RRID: AB_395799
Mouse monoclonal anti-human CD19, PE	BD Bioscience	Cat# 555413; RRID: AB_395813
Mouse monoclonal anti-human CD45, KrO	Beckman Coulter	Cat# A96416; RRID: AB_2888654
Mouse monoclonal anti-huamn CD19, APC	BD Bioscience	Cat# 555415; RRID: AB_398597
Mouse monoclonal anti-human TACSTD2 (TROP2), PE	Biolegend	Cat# 363804; RRID: AB_2572022
Rat monoclonal anti-GFP, Alexa Fluor 488	Biolegend	Cat# 338008; RRID: AB_2563288
Mouse monoclonal anti-His Tag, PE	Biolegend	Cat# 362603; RRID: AB_2563634

(*Continued on next page*)

Please cite this article in press as: Li et al., Depletion of an immature cord blood NK subset reverses trogocytosis-driven CAR NK dysfunction, Cancer Cell (2026), https://doi.org/10.1016/j.ccell.2026.06.017

Continued

REAGENT or RESOURCE	Source	IDENTIFIER
Human CD20/MS4A1 Full Length Protein, His Tag	ACROBiosystems	Cat# CD0-H52H1-100 μg
Biotinylated anti-human SLAMF7/CRACC/CD319 Protein, Avitag, His Tag	ACROBiosystems	Cat# SL7-H82E0-200 μg
Donkey polyclonal anti-rabbit IgG, PE	Biolegend	Cat# 406421; RRID: AB_2563484
7-AAD vialibility staining solution	Biolegend	Cat# 79993
eBioscienc fixable viability dye eFluor 506	Invitrogen	Cat# 65-0866-14
LIVE/DEAD fixable blue dead cell stain kit	Invitrogen	Cat# L23105 A
LIVE/DEAD fixable aqua dead cell stain kit	Invitrogen	Cat# L34966 A
UltraComp eBeads plus compensation beads	Invitrogen	Cat# 01-3333-421
FAM-FLICA caspase-1 kit	BIO-RAD	Cat# ICT098
True-Stain monocyte blocker	BioLegend	Cat# 426101
Fcr Blocking reagent human	Miltenyi Biotec	Cat# 130-059-901; RRID: AB_2892112
Recombinant human monoclonal IgG1 anti-CD20, PE	Miltenyi Biotec	Cat# 130-111-338; RRID: AB_2656080
TotalSeq-C5100 custom oligo conjugation	Biolegend	Cat# 900010178
Mouse monocolonal TotalSeq-C1290 anti-human CD3	Biolegend	Cat# 300341; RRID: AB_3083166
Mouse monocolonal TotalSeq-C0166 anti-human CD66b	Biolegend	Cat# 392909; RRID: AB_2801027
Mouse monocolonal TotalSeq-C0100 anti-human CD20	Biolegend	Cat# 302363; RRID: AB_2800743
Mouse monocolonal TotalSeq-C0052 anti-human CD33	Biolegend	Cat# 366633; RRID: AB_2801008
Mouse monocolonal TotalSeq-C0051 anti-human CD14	Biolegend	Cat# 367137; RRID: AB_2810576
Mouse monocolonal TotalSeq-C0050 anti-human CD19	Biolegend	Cat# 302265; RRID: AB_2800741
Mouse monocolonal TotalSeq-C0048 anti-human CD45	Biolegend	Cat# 368545; RRID: AB_2801014
Mouse monocolonal TotalSeq-C0047 anti-human CD56	Biolegend	Cat# 362559; RRID: AB_2801002
Mouse monocolonal TotalSeq-C0083 anti-human CD16	Biolegend	Cat# 302065; RRID: AB_2800738
Mouse monocolonal TotalSeq-C0149 anti-human CD161	Biolegend	Cat# 339947; RRID: AB_2810532
Mouse monocolonal TotalSeq-C0251 anti-human Hashtag 1	Biolegend	Cat# 394661; RRID: AB_2801031
Mouse monocolonal TotalSeq-C0252 anti-human Hashtag 2	Biolegend	Cat# 394663; RRID: AB_2801032
Mouse monocolonal TotalSeq-C0253 anti-human Hashtag 3	Biolegend	Cat# 394665; RRID: AB_2801033
Mouse monocolonal TotalSeq-C0254 anti-human Hashtag 4	Biolegend	Cat# 394667; RRID: AB_2801034
Stain cell membrane 405	Bruker Cellular Analysis	Cat# STAIN-1001-1
Cell-ID Cisplatin-194Pt	Standard BioTools	Cat# 201194
Cell-ID Intercalator-Ir	Standard BioTools	Cat# 201192 A
Ghost dye UV 450	Tonbo Biosciences	Cat# 13-0868-T100
Mouse Anti-Human CD45-89Y	Standard BioTools	Cat# 3089003 B; RRID: AB_2938863
Recombinant human monoclonal IgG1 anti-CD196	Miltenyi Biotec	Cat# 130-108-023; RRID: AB_2904799

(*Continued on next page*)

Continued

REAGENT or RESOURCE	Source	IDENTIFIER
Recombinant human monoclonal IgG1 anti-CD20	Miltenyi Biotec	Cat# 130-124-537; RRID: AB_2656080
Mouse monoclonal anti-human CD19	Biolegend	Cat# 302202; RRID: AB_314232
Mouse monoclonal anti-human Zap-70	Thermo Fisher Scientific	Cat# 14-6695-82; RRID: AB_468191
Rat monoclonal anti-GFP	Biolegend	Cat# 338002; RRID: AB_1279415
Recombinant human monoclonal IgG1 anti-Granzyme A	Miltenyi Biotec	Cat# 130-108-054; RRID: AB_2889676
Mouse monoclonal anti-human DAP12	R&D Systems	Cat# MAB52401; RRID: AB_3658432
Mouse monoclonal anti-human CD159c	R&D Systems	Cat# MAB138; RRID: AB_2132982
Recombinant human monoclonal IgG1 anti-CD158f	Miltenyi Biotec	Cat# 130-126-477; RRID: AB_2727257
Mouse monoclonal anti-human KIR3DL1	BD Bioscience	Cat# 555964; RRID: AB_396258
Recombinant human monoclonal IgG1 anti-CD158a	Miltenyi Biotec	Cat# 130-122-279; RRID: AB_2752103
Mouse monoclonal anti-human CD158b	Miltenyi Biotec	Cat# 130-092-615; RRID: AB_2660192
Recombinant human monoclonal IgG1 anti-CD158b2	Miltenyi Biotec	Cat# 130-122-280; RRID: AB_2904747
Recombinant human monoclonal IgG1 anti-CD25	Miltenyi Biotec	Cat# 130-122-302; RRID: AB_2726346
Mouse monoclonal anti-human CD69	Biolegend	Cat# 310902; RRID: AB_314837
Mouse monoclonal anti-human Syk	Biolegend	Cat# 644301; RRID: AB_2200267
Recombinant mouse monoclonal anti-human TIGIT	Thermo Fisher Scientific	Cat# 740010 M; RRID: AB_2942255
Recombinant human monoclonal IgG1 anti-CD158i	Miltenyi Biotec	Cat# 130-122-328; RRID: AB_2655368
Rabbit Recombinant monoclonal IgG anti-human CD158h	R&D Systems	Cat# MAB8887; RRID: AB_2893529
Recombinant human monoclonal IgG1 anti-CD158d	Miltenyi Biotec	Cat# 130-126-474; RRID: AB_3664293
Mouse monoclonal anti-human KIR2DL3	R&D Systems	Cat# FAB1848CL1; RRID: AB_2130575
Rat monoclonal anti-human CX3CR1	Biolegend	Cat# 341602; RRID: AB_1595422
Mouse anti-human CD183-156Gd	Standard BioTools	Cat# 3156004 B; RRID: AB_2687646
Recombinant human monoclonal IgG1 anti-CD134	Miltenyi Biotec	Cat# 130-109-600; RRID: AB_2928235
Anti-his antibody	Miltenyi Biotec	Cat# 130-133-293; RRID: AB_2876894
Recombinant human monoclonal IgG1 anti-T-bet	Miltenyi Biotec	Cat# 130-122-287; RRID: AB_2784466
Rat monoclonal anti-human TIM3	R&D Systems	Cat# MAB2365; RRID: AB_2232900
Mouse monoclonal anti-human EOMES	Thermo Fisher Scientific	Cat# 14-4877-82; RRID: AB_2572882
Recombinant human monoclonal IgG1 anti-HLA-DR	Miltenyi Biotec	Cat# 130-122-299; RRID: AB_2801880
Mouse Anti-human CD95-164Dy	Standard BioTools	Cat# 3164008 B; RRID: AB_2858235
Recombinant human monoclonal IgG1 anti-CD279	Miltenyi Biotec	Cat# 130-096-168; RRID: AB_2733366
Recombinant human monoclonal IgG1 anti-CD314	Miltenyi Biotec	Cat# 130-122-332; RRID: AB_2657366
Mouse monoclonal anti-human CD244	Thermo Fisher Scientific	Cat# 16-5838-85; RRID: AB_657715
Mouse monoclonal anti-human Ki-67	Biolegend	Cat# 350501; RRID: AB_10662749
Recombinant human monoclonal IgG1 anti-CD159a	Miltenyi Biotec	Cat# 130-122-329; RRID: AB_2726450
Mouse monoclonal anti-human CD3	Biolegend	Cat# 300401; RRID: AB_314055

(*Continued on next page*)

Please cite this article in press as: Li et al., Depletion of an immature cord blood NK subset reverses trogocytosis-driven CAR NK dysfunction, Cancer Cell (2026), https://doi.org/10.1016/j.ccell.2026.06.017

Continued

REAGENT or RESOURCE	Source	IDENTIFIER
Recombinant human monoclonal IgG1 anti-CD226	Miltenyi Biotec	Cat# 130-126-485; RRID: AB_2727961
Recombinant human monoclonal IgG1 anti-KLRG1	Miltenyi Biotec	Cat# 130-126-458; RRID: AB_2733431
Mouse monoclonal anti-human CD184/ CXCR4-173Yb	Standard BioTools	Cat# 3173001 B; RRID: AB_3106963
Rat monoclonal anti-mouse CD45	Biolegend	Cat# 103101; RRID: AB_312966
Recombinant human monoclonal IgG1 anti-CD161	Miltenyi Biotec	Cat# 130-122-347; RRID: AB_2922140
Recombinant human monoclonal IgG1 anti-LAG3	Miltenyi Biotec	Cat# 130-124-529; RRID: AB_2784076
Recombinant human monoclonal IgG1 anti-CD278	Miltenyi Biotec	Cat# 130-122-304; RRID: AB_2921752
Mouse anti-human CD16-209Bi	Standard BioTools	Cat# 3209002 B; RRID: AB_2756431
Recombinant human monoclonal IgG1 anti-CD57	Miltenyi Biotec	Cat# 130-124-525; RRID: AB_2658747
Recombinant human monoclonal IgG1 anti-CD39	Miltenyi Biotec	Cat# 130-093-506; RRID: AB_2922147
Recombinant human monoclonal IgG1 anti-Perforin	Miltenyi Biotec	Cat# 130-126-480; RRID: AB_2733891
Recombinant human monoclonal IgG1 anti-Granzyme B	Miltenyi Biotec	Cat# 130-108-055; RRID: AB_2733663
Mouse monoclonal anti-human CD56	BD Bioscience	Cat# 559043; RRID: AB_397180
Recombinant human monoclonal IgG1 anti-CD19 CAR FMC63	Miltenyi Biotec	Cat# 130-127-983: RRID: AB_3664158
Donkey anti-Mouse IgG (H + L)	Jackson Immune Research	Cat# 715-005-150; RRID: AB_2340758
Mouse monoclonal anti-human CD2	R&D Systems	Cat# NBP2-25200; RRID: AB_2244323
Recombinant human monoclonal IgG1 anti-CD8a	Miltenyi Biotec	Cat# 130-122-281; RRID: AB_2659234
Mouse monoclonal anti-human CD337	Miltenyi Biotec	Cat# 130-092-554; RRID: AB_2819620
Recombinant human monoclonal IgG1 anti-CD335	Miltenyi Biotec	Cat# 130-124-522; RRID: AB_2734017
Recombinant human monoclonal IgG1 anti-CD336	Miltenyi Biotec	Cat# 130-126-465; RRID: AB_2784138
Bacterial strains		
Stellar competent cells	Takara Bio	Cat# 636763
Biological samples		
Human cord blood-derived natural killer cells	The University of Texas MD Anderson Cancer Center Cord Blood Bank	IRB-approved protocol Lab04-0249
Chemicals, reagents		
Ampicillin sodium salt	Sigma-Aldrich	Cat# A5354-10ML
DMEM	Gibco	Cat# 11965118
Penicillin-Streptomycin	Gibco	Cat# 15140122
RPMI 1640	Cytiva	Cat# SH30096.01
TrypLE express enzyme	Gibco	Cat# 12-604-021
100 mM pyruvate solution	Agilent Technologies	Cat# 103578-100
Poly-L-Ornithine	Sigma-Aldrich	Cat# P4957
1.0 M glucose solution	Agilent Technologies	Cat# 103577-100
Glutamax	Gibco	Cat# 35050-061
Dulbecco's Phosphate Buffered Saline (DPBS)	Cytiva	Cat# SH30028.02

(*Continued on next page*)

Please cite this article in press as: Li et al., Depletion of an immature cord blood NK subset reverses trogocytosis-driven CAR NK dysfunction, Cancer Cell (2026), https://doi.org/10.1016/j.ccell.2026.06.017

Continued

REAGENT or RESOURCE	Source	IDENTIFIER
DMEM	Cytiva	Cat# SH30022.01
Click's Medium (EHAA)	FUJIFILM Biosciences	Cat# 9195
Opti-MEM	Gibco	Cat# 31985070
BD Pharm Lyse Lysing Buffer	BD Biosciences	Cat# 555899
Lymphoprep	Serumwerk Bernburg	Cat# 1856
CD235a (Glycophorin A) microbeads	Miltenyi Biotec	Cat# 130-050-501
DMSO	Invitrogen	Cat# L23105 B
Miller's LB broth	Corning	Cat# 34524003
Accucheck counting beads	Invitrogen	Cat# PCB100
Protector RNase inhibitor	Sigma-Aldrich	Cat# 3335402001
1,4-Dithiothreitol (DTT)	Sigma-Aldrich	Cat# 10708984001
FluoroBrite DMEM	Thermo Fisher Scientific	Cat# A1896701
Bovine serum albumin In DPBS (10%)	Sigma-Aldrich	Cat# A1595
UltraPure bovine serum albumin	Thermo Fisher Scientific	Cat# AM2616
Formaldehyde (37%)	Thermo Fisher Scientific	Cat# BP531-25
Nuclease-free water (not DEPCTreated)	Thermo Fisher Scientific	Cat# AM9937
ViaStain AOPI staining solution	Nexcelom bioscience	Cat# CS2-0106-25ML
Tween 20	Thermo Fisher Scientific	Cat# 28320
DNA LoBind Tubes 2.0 mL	Eppendorf	Cat# 022431048
1.5mL DNA LoBind tubes	Eppendorf	Cat# 022431021
Glycerol	Sigma-Aldrich	Cat# G5516-100ML
Glycine	Sigma-Aldrich	Cat# 3570-500GM
Magnesium chloride solution	Sigma-Aldrich	Cat# M1028–10X1ML
Maxpar fix and perm buffer	Standard BioTools	Cat# 201067
LS columns	Miltenyi Biotec	Cat# 130-042-401
Tryple express enzyme (1×), no phenol red	Gibco	Cat# 12604021
AccuCheck counting beads	Invitrogen	Cat# PCB100
Halt protease inhibitor cocktail (100×)	Thermo Fisher Scientific	Cat# 1861278
Critical commercial assay		
Seahorse XFe96/XF pro cell culture microplates	Agilent Technologies	Cat# 103794-100
Seahorse XFe96/XF pro fluxPak mini	Agilent Technologies	Cat# 103793-100
Seahorse XF Cell Mito Stress test kit	Agilent Technologies	Cat# 103015-100
Seahorse XF Glycolysis Stress test kit	Agilent Technologies	Cat# 103020-100
Seahorse XF calibrant solution 500 mL	Agilent Technologies	Cat# 100840-000
Cyto-Fast Fix/Perm buffer set	BioLegend	Cat# 426803
FuGENE HD transfection reagent	Fugene HD	Cat# E2312
Applied biosystems fast SYBR green master mix	Applied Biosystems	Cat# 4385612
iScript cDNA synthesis kit	Bio-Rad Laboratories	Cat# 1708891
Chromium next GEM single cell fixed RNA sample preparation kit	10× Genomics	Cat# 1000414
GEM-X FX chip	10× Genomics	Cat# 2001257
Dual Index Kit TS Set A	10× Genomics	Cat# 1000251
Dual Index Kit TN Set A	10× Genomics	Cat# 1000250
GEM-X Flex gene expression chip kit	10× Genomics	Cat# 1000791
Fixed RNA feature barcode multiplexing kit	10× Genomics	Cat# 1000628
GEM-X Flex supplemental wash Kit	10× Genomics	Cat# 1000828
GEM-X Flex Gene expression human 4-plex	10× Genomics	Cat# 1000793
GEM-X Flex sample preparation v2 Kit	10× Genomics	Cat# 1000781

(*Continued on next page*)

Please cite this article in press as: Li et al., Depletion of an immature cord blood NK subset reverses trogocytosis-driven CAR NK dysfunction, Cancer Cell (2026), https://doi.org/10.1016/j.ccell.2026.06.017

Continued

REAGENT or RESOURCE	Source	IDENTIFIER
RNeasy plus mini kit	QIAGEN	Cat# 74134
DNeasy blood & tissue kit	QIAGEN	Cat# 69504
NK cell isolation kit, human	Miltenyi Biotec	Cat# 130-092-657
Taqman copy number reference assay, human, RNase P	Thermo Fisher Scientific	Cat# 4403326
Single-cell natural killer panel - (H) 8	Bruker Cellular Analysis	Cat# PANEL-3L03-8
Absolute Q DNA digital PCR master mix	Thermo Fisher Scientific	Cat# A52490
Deposited data		
Single cell RNA seq data of pre-manufactured/primary human NK cells	This paper	Figure 2; Figure S2/GSE313836
Single cell RNA +ADT seq data of *ex vivo* expanded human NK cells	This paper	Figure 3; Figures S4 and S5/GSE313836
Transcriptome data derived from GEM-flex single cell sequencing used in the generation of Figures 2 and 3 are available through the Gene Expression Omnibus under accessions GSE313836. No custom code was developed for this research article.	This paper	https://www.ncbi.nlm.nih.gov/geo/
Experimental models: Cell lines		
HEK293T	ATCC	CRL-3216
Raji	ATCC	CCL-86
SKOV3	ATCC	HTB-77
K562	ATCC	CRL-243
Experimental models: Organisms/strains		
Mouse: NOD.Cg-Prkdcscid Il2rgtm1Wjl/SzJ	The Jackson Laboratory	RRID: IMSR_JAX:005557
Software and algorithms		
FlowJo version 10.10	Becton Dickinson & Company (BD)	https://www.flowjo.com/
Morpheus	Broad Institute	https://software.broadinstitute.org/morpheus
PRISM version 10.4.0	GraphPad Software, LLC	https://www.graphpad.com
bioRender	Biorender	https://www.biorender.com
Adobe Illustrator 2025 version 29.0.1	Adobe Inc.	https://www.adobe.com/
CytoBank	Beckman Coulter	https://premium.cytobank.org/
LasX software	Leica	https://www.leica-microsystems.com/
incucyte	Satorius	https://www.sartorius.com/

EXPERIMENTAL MODEL AND STUDY PARTICIPANT DETAILS

Cell lines, primary cells, and culture conditions

Cell lines including Raji (CCL-86), SKOV3 (HTB-77), K562 (CCL-243), and 293 T (CRL-3216) were obtained from the American Type Culture Collection (ATCC). Raji and K562 cells were cultured in RPMI-1640 (Invitrogen) supplemented with 10% fetal bovine serum (FBS; Corning), 1% penicillin-streptomycin (Gibco), and 1% GlutaMAX (Gibco). 293Tcells were cultured in DMEM (Thermo Fisher) supplemented with 10% FBS, 1% penicillin-streptomycin, and 1% GlutaMAX. SKOV3 cells were cultured in McCoy's 5a Medium (Invitrogen) supplemented with 10% FBS, 1% penicillin-streptomycin, and 1% GlutaMAX. K562 cells were retrovirally transduced to co-express 4-1BBL, CD48, and membrane-bound interleukin (IL)-21, and served as universal antigen-presenting cells (uAPCs) for *in vitro* NK cell expansion.[1] To model trogocytosis detection using a fluorescent traceable marker, a CD19-mCherry fusion protein was retrovirally transduced into targeted cells. Additionally, tumor cells were transduced with firefly luciferase-GFP to facilitate detection of target cells versus effectors, and to enable *in vivo* tumor burden assessment using the IVIS Spectrum imaging system (Caliper). All cells were maintained in a 37°C incubator with 5% CO_2 and were routinely tested for mycoplasma contamination using the MycoAlert Mycoplasma Detection Kit (Lonza), and all samples consistently tested negative.

Manufacture of CAR NK cells from CBUs

The clinical cord blood units (CBU) used for CAR NK cell products were obtained from the MD Anderson Cord Blood Bank. CBUs were collected with informed consent from mothers at several hospitals and shipped to the MD Anderson Cord Blood Bank for processing and cryopreservation, following established standard operating procedures. CBUs from each donor used for CAR NK product manufacturing for the clinical trial (ClinicalTrials.gov identifier: NCT03056339) were cryopreserved in advance as reference material for quality evaluation. For research purposes, selected CBUs were delivered to the research facility, and CAR NK cells were manufactured under an IRB-approved protocol (Lab04-0249). Briefly, each cord unit was thawed in a 37°C water bath, and cord blood mononuclear cells (CBMCs) were collected by density-gradient centrifugation using Ficoll-Histopaque solution (Sigma-Aldrich). $CD56^+CD3^-$ NK cells were then purified using an NK cell isolation kit (Miltenyi Biotec), expanded and cultured in the presence of engineered uAPCs, along with exogenous IL-2 (200 U/mL; Proleukin, Merck). NK cell subsets were flow sorted based on their phenotype of $CD56^+CD3^-CD14^-CD33^-$ as well as their differential surface CD16 and CD161 expression prior *ex vivo* expansion. On day 6 of culture, cells were transduced with a retroviral vector encoding CARs targeting CD19 (kindly provided by Dr. Gianpietro Dotti, University of North Carolina - Chapel Hill[2]), CD20 (clone: Leu-16), or TROP2 (clone: hRS7), respectively, along with IL-15 and iC9 genes. For some conditions, NK subsets were subjected to preactivation using rhIL-12 (10ng/mL; Biolegend), rhIL-18 (50ng/mL; MBL International), and rhIL-15 (50ng/mL; Biolegend) overnight, with or without the following *ex vivo* expansion with uAPC. The cells were then expanded for use in subsequent experiments.

METHOD DETAILS

Cell preparation for single-cell RNA sequencing

Primary CBMCs from thawed CBUs after purification of CBMCs via Ficoll density-gradient centrifugation were freshly prepared, and then were resuspended in PBS containing 0.04% BSA. Cell viability was assessed using 0.4% Trypan Blue staining with the Countess II FL automated cell counter. Cells were diluted or concentrated to the recommended range of 500-1,000 cells/μL and loaded at a volume targeting the recovery of 7,000–10,000 cells per sample for single-cell RNA sequencing (scRNA-seq). To prepare the expanded NK cell subsets. NK cells were first isolated from thawed CBUs after purification of CBMCs via Ficoll density-gradient centrifugation, as described above. The isolated NK cells were then subjected to FACS to obtain purified NK cell subsets. First, Fc receptors were blocked using Human TruStain FcX (BioLegend; 1:50) for 15 min at 4°C. Cells were then stained for 30 min at 4°C with the following fluorochrome-conjugated antibodies: anti-human CD45-Krome Orange (Beckman Coulter; 1:40), DAPI (ThermoFisher; 1:1000), anti-human CD56-BV510 (Biolegend; 1:200), anti-human CD16-FITC (Biolegend; 1:100), anti-human CD161-APC (Miltenyi Biotec; 1:100), anti-human CD3-PE (Biolegend; 1:200), anti-human CD33-PE (Biolegend; 1:200), and anti-human CD14-PE (Biolegend; 1:200). Live $CD56^+CD3^-CD33^-CD14^-$ NK cells were sorted into subsets expressing both CD16 and CD161, denoted as the double positive (DP) NK cell subset; or subsets that lacked both CD16 and CD161 expression, denoted as the double negative (DN) NK cell subset. Sorted NK cell subsets were expanded by co-culture with uAPCs and exogenous IL-2 (200 U/mL) for two weeks. DP/DN-derived NK cells were then stained with combinations of the following nucleotide barcode-labeled antibodies (BioLegend) for epitope labeling: TotalSeq-C1290 anti-human CD3 (HIT3a; 1:200), TotalSeq-C0168 anti-human CD57 (QA17A04; 1:200), TotalSeq-C0166 anti-human CD66b (6/40c; 1:200), TotalSeq-C0100 anti-human CD20 (2H7; 1:200), TotalSeq-C0083 anti-human CD16 (3G8; 1:200), TotalSeq-C0051 anti-human CD14 (63D3; 1:200), TotalSeq-C0050 anti-human CD19 (HIB19; 1:200), TotalSeq-C0251 anti-human Hashtag 1 (2M2; 1:200), TotalSeq-C0252 anti-human Hashtag 2 (2M2; 1:200), TotalSeq-C0253 anti-human Hashtag 3 (2M2; 1:200), TotalSeq-C0254 anti-human Hashtag 4 (2M2; 1:200), TotalSeq-C0052 anti-human CD33 (P67.6; 1:150), TotalSeq-C0048 anti-human CD45 (2D1; 1:150), TotalSeq-C5100-custom-CD161 (REA631; 1:150), TotalSeq-C0047 anti-human CD56 (5.1H11; 1:150), TotalSeq-C0149 anti-human CD161 (HP-3G10; 1:150). As described in the GEM-X Flex gene expression protocols provided by the manufacturer (10× Genomics), cells were fixed with fixation buffer overnight in 4°C. Fixation was quenched with additive C and quenching buffer. Cells were then washed twice with quenching buffer and counted, 500,000 cells from each sample were loaded.

Single-cell library preparation for GEX and ADT

For primary CBMCs, Single-cell capture, barcoding, and library preparation were performed according to the 10× Genomics Chromium Next GEM Single Cell 3′ v3.1 Reagent Kits protocol (CG000204 Rev D). Ten libraries were pooled to a final concentration of 10 nM. The pooled libraries were further quantified by qPCR prior to sequencing. Sequencing was performed on an Illumina NovaSeq 6000 using an S2 100-cycle flow cell using R1-i7-R2 parameters of 28 + 8+91 cycles. Sequencing was conducted at the ATGC Core Facility at MD Anderson. For expanded DN, and DP cells, libraries were prepared using the GEM-X Flex Gene Expression Reagent Kit (10× Genomics) following the manufacturer's instructions. Briefly, each sample was subjected to probe hybridization for their gene expression (GEX) and TotalSeq antibody-derived epitope tags (ADT), respectively. Samples were then pooled for GEM generation and subsequent library preparation of both GEX and ADT fractions. Library size and quality were determined using a Fragment Analyzer (Agilent TapeStation Traces) before fragmentation and after final purification. Final library concentrations were measured using a Qubit 2.0 fluorometer (Thermo Fisher). For each sequencing reaction, pooling was performed with the aim of achieving ~30,000 reads per cell for the GEX libraires and ~10,000 reads per cell for the ADT libraries. The pooled GEM-X Flex libraries were sequenced on the Illumina NovaSeq X Plus instrument using R1-i7-i5-R2 parameters of 28 + 10+10 + 90 cycles.

Please cite this article in press as: Li et al., Depletion of an immature cord blood NK subset reverses trogocytosis-driven CAR NK dysfunction, Cancer Cell (2026), https://doi.org/10.1016/j.ccell.2026.06.017

10× genomics chromium 3′ scRNA-seq data preprocessing and analysis for CB-NK cell

Raw sequencing reads were demultiplexed and aligned to the human reference genome GRCh38.p12[45,46] using the 10× Genomics Cell Ranger pipeline (v6.1.2)[47] for scRNA-seq data preprocessing. Gene expression count matrices were further processed and analyzed using Seurat (v5.4.0).[48] Cells with 1) fewer than 500 detected genes, 2) higher than 5000 genes, and 3) greater than 10% mitochondrial gene expression were excluded to remove low-quality, damaged, or dead cells. Samples were then merged for doublets identification using scDblFinder with default settings[49] and cell type annotation using Azimuth with PBMC as reference (https://satijalab.org/azimuth/). Azimuth Level 1 broad annotation with a certainty higher than 0.8 as NK cells and singlets were kept for downstream analysis.

Cells were split by sample identity prior to normalization to preserve sample-level structure using Seurat pipeline. Gene expression values were log-normalized, and highly variable features were identified using default parameters. Data were scaled across all genes, followed by principal component analysis (PCA). Cell-cell similarity was computed using the top 30 principal components, and clustering was performed using a shared nearest neighbor graph with Louvain optimization (resolution = 0.3). Low-dimensional embedding was generated using Uniform Manifold Approximation and Projection (UMAP). No batch correction was applied as no batch effect from sample pooling was observed. Cluster identity was then evaluated using our marker genes, including *FCGR3A*, *KLRB1*, *NCAM1*, and *MKI67*. A low-quality or contaminating cluster with less than 100 cells was removed, and the dataset was reprocessed using the same workflow, with clustering performed at a resolution of 0.2. Definition of $CD16^{-}$and CD161-postive cells were based on cutoffs of 1.2 and 2.1, respectively, based on RNA assay. Cluster-specific marker genes were identified using Seurat by testing differential expression across all clusters. Genes expressed in at least 10% of cells were considered, and significance was defined as an adjusted p-value <0.05 with an absolute log2 fold-change more than log2(1.2). Top-ranked marker genes for each cluster were selected based on effect size to facilitate cluster annotation and biological interpretation. Those genes were also subjected to over-representation analysis using curated gene sets derived from MSigDB (i.e., the Hallmark collection, Reactome, and GOBP). Enrichment was performed using grouped gene lists corresponding to each cluster, with significance determined by multiple testing correction (FDR<0.05) and top 30 enriched functions per cluster visualized using emapplot function from clusterProfiler R package.[50] Signature scores for NK cell activation, inhibition, cytotoxicity, and inflammation were computed using R package AUCell as above.

NK cell clusters (CBNK-C1, -C4 and -C5) were selected for trajectory analysis. Cells were converted to a SingleCellExperiment object, and lineage inference was performed using Slingshot[51] on UMAP embeddings with cluster labels provided by Seurat. Pseudotime values were computed for each lineage without imposing a predefined root. To identify genes associated with dynamic changes along pseudotime, generalized additive models were fit using tradeSeq.[52] Genes with significant association to pseudotime (FDR less than 0.05, log2 fold-change more than 1) were retained for downstream analysis. Smoothed gene expression profiles were computed across pseudotime and scaled per gene for visualization.

To assess higher-order relationships between gene modules, Mantel tests were performed to quantify the association between distance matrices derived from two distinct gene sets. Specifically, top 20 differentiated expression profiles of NK cell surface markers (“*KLRB1*”, “*KLRC1*”, “*CD160*”, “*CD226*”, “*SEMA4D*″, “*IL7R*″, “*IL2RG*”, “*XCL1*”, “*CCL3*”, “*CCL4*”, “*CCL5*”, “*HCST*”, “*TYROBP*”, “*CD7*”, “*CD44*”, “*FCGR3A*″, “*ITGB2*”, “*KLRF1*”, “*KLRK1*”, “*TGFBR3*”) and cluster-associated top 5 marker gene list that was partitioned into predefined cluster groups, and distance matrices were computed using default metrics, respectively. Mantel statistics were calculated to evaluate the correlation between these two dissimilarity matrices. Significance thresholds for Mantel correlation coefficients (r) and associated p-values were applied to stratify interaction strength and statistical confidence. Results were visualized by overlaying Mantel test statistics onto gene-gene correlation structures and were jointly visualized with network-like connections representing significant associations between gene modules.

Preprocessing of single cell GEX and ADT data for expanded NK cell subsets

Sequencing raw data were converted into fastq files by running Illumina’s bcl2fastq. The data were aligned to reference genome (GRCh38-2024-A) using Cell Ranger (10× Genomics Cell Ranger 9.0.1). After mapping, Seurat was used as the primary R package for quality control, transformation and most of the visualization of the gene expression data.[53] Quality control steps were first carried out using GEX assay whereby cells not expressing a minimum of 500 genes and genes expressed less than 3 cells were removed. The number of genes expressed, and the percentage of mitochondrial reads mapped were capped at 7500 and 5%, respectively. Doublets were filtered out using the scDblFinder R package.[49] Cells were then annotated based on reference-based mapping against the human PBMC ref.[54] using Azimuth R package.[55] Any cells mapped to NK cell type with more than 80% of certainty were retained. The GEX data were normalized using log(transformation) for some of the downstream analysis as well as for visualization of gene expression-like heatmaps. Cell cycle phases were identified using Seurat by scoring cells based on canonical markers of the S and G2/M phases with the *CellCycleScoring* function. Cells were then classified into G1, S, or G2/M phases based on their relative expression of these marker gene sets. A further data-cleaning step based on ADT assay was performed using its centered log ratio (CLR) normalized data. Cells expressing any of the non-NK lineage markers (i.e., CD3, CD66b, CD20, CD33, CD14, CD19) more than 0.5 were filtered out. The remaining cells were used for dimensionality reduction and clustering. Batch effects were visualized and examined carefully. R package Harmony[56] was then used for integration of DP/DN NK scRNA-seq data by sex and cell cycling phases to remove unwanted variations. DP-NK and DN-NK were processed and analyzed, separately, according to the above procedures. Cluster marker analysis using the GEX assay was performed using the Seurat package to identify genes specifically enriched in each cell cluster. Differentially expressed genes were determined with the *FindAllMarkers* function with min.pct set as 0.2, comparing each cluster against all others to define representative marker genes for downstream cell cluster annotation and functional interpretation.

Please cite this article in press as: Li et al., Depletion of an immature cord blood NK subset reverses trogocytosis-driven CAR NK dysfunction, Cancer Cell (2026), https://doi.org/10.1016/j.ccell.2026.06.017

Definition of CD16-positive and CD161-positive cells were based on cutoffs of 0.7 and 1.6, respectively, based on the ADT assay. Signature scores were computed using R package AUCell,[57] allowing for exploration of the relative expression of gene sets of interest in our data. Reactome related gene sets under immune category were taken from the MSigDB collection[58] and used for cell-based scoring. Meanwhile, NK cell activation, inhibition, cytotoxicity, and inflammatory gene signatures were defined based on curated marker genes from prior studies of NK cell biology and immune regulation. The NK activation gene set included *CD244, CD226, KLRC2, KLRK1, NCR3, NCR1, NCR2, CD69, IL2RA, KIR2DS1, KIR2DS2, KIR2DS4, FCGR3A, LAMP1*, and *KIT*. Gene sets to evaluate the activation signaling strengthen through membrane-proximity elements included *KLRC1, KLRC2, NCR1, NCR2, NCR3, KLRK1, CD244, CD226, SLAMF7, FCGR3A, TYROBP, CD247, TNFRSF9, ZAP70, LAT, LCK, VAV1*, as well as the activation signaling strengthen through endosomal components included *TLR3, TLR7, TLR8, TLR9, DDX58, IFIH1, STING1, ZBP1, TREX1, MYD88, TRIF, IRAK1, IRAK4, TRAF6, TBK1, IKBKE, IRF3, IRF7, IRF9, IFNAR1, IFNAR2, MX1, ISG15, OAS1, IFITM2, IFIT1, IFIT3, CSF2RB*. The NK inhibition gene set included *KIR2DL2, KIR2DL3, KLRD1, KLRC1, KIR3DL1, SIGLEC7, LAG3, HAVCR2, TIGIT, PDCD1*, and *LILRB1*. The cytotoxicity gene signature consisted of canonical effector molecules: *TNFSF10, PRF1, SYK, ZAP70, GZMB, GZMA, FAS, CD247, GZMH, GZMM, GZMK, CTSW, IFNG*, and *GNLY.* To assess the potential of immune cells in regulating immunological synapse, we defined a cytoskeleton and immunological synapse gene set including *ITGAL, ITGB2, FERMT3, SEMA4D, AKAP9, ACTB, WAS, ARPC1B, CDC42, RAC1, RAC2, DOCK2, DOCK8, CORTACTIN, KIF1B, SH2D1A, ADAP, LCP2, VAV1, VAV2, VAV3, NCK1, NCK2*. To assess inflammatory signaling and homing potential, we defined an inflammatory chemokine receptor gene set including *CCR2, CCR5, CCR7, CXCR1, CXCR6, CXCR3, CXCR4, CX3CR1, CCR4*, and *S1P5*.

DN/DP-specific and -unique signatures

To derive DN/DP gene signatures, we performed differentially expressed gene (DEG) analysis between the group of DN and DP NK cells using the pseudobulk method.[59] This allowed us to aggregate up counts for each sample and consider the samples per DN or DP group as replicates instead of the single cells. We then used DESeq2[60] on the pseudobulk data. We could then identify DEGs between DN and DP groups to define DN/DP-specific and -unique signatures for visualization.

CAR NK cell population doubling assay

CAR NK cells generated by transduction were subcultured every week with fresh uAPC feeder cells + IL-2 (200 U/mL). Using the equation for population doubling (PD) = Log_2 (A/B), where A is the number of harvested cells and B is the number of plated cells from each subculture, weekly PD was measured. Cumulative PD was defined as the sum of PDs over time of each subculture.

IsoPlexis assay

The single-cell secretome analysis was performed using the IsoCode chip from IsoPlexis using the human NK cytokine panel by following the manufacturer's instructions. In brief, CAR19 NK cells were stimulated by culturing in plates coated with cognate antigen CD19 (ACRO, CD19-H5259; 10 μg/mL) for 6 h at 37°C prior to the assay. Cells were then labeled with a fluorescent dye (IsoPlexis stain cell membrane 405) for loading. A total of 30,000 cells per condition were loaded onto each IsoCode chip. The IsoLight device was used to scan the chips, followed by data analysis using IsoPlexis' proprietary IsoSpeak software. Polyfunctionality and the polyfunctionality strength index (PSI), as computed by the software, represent the number of cytokines detected from each cell event, and their function definition: Effector PSI comprising GrB, IFN-γ, MIP-1α, perforin, TNF-α and TNF-β; Chemokine PSI comprising CCL-11, IP-10, MIP-1β and RANTES; and Regulatory PSI comprising IL-10, IL-3, IL-22, IL-4, sCD137, sCD40L and TGF-β1.

IFN-γ secretion assay

The IFN-γ secretion assay was performed using the Human IFN-γ ELISA Kit (Invitrogen) according to the manufacturer's instructions. Briefly, NK cells were stimulated by coculture with tumor cells that had been previously infected with either HSV (G207, kindly provided by Dr. Gregory Friedman's lab, MDACC) or adenovirus (Delta-24-RGD, kindly provided by Dr. Juan Fueyo and Dr. Candelaria Gomez-Manzano, MDACC), or by stimulation with TLR agonists: LPS-B5 (TLR4 agonist, 500 pg/mL; InvivoGen), ORN06/LyoVec (TLR7/8 agonist, 5 μg/mL; InvivoGen), ODN 1585 (TLR9 agonist, 5 μM; InvivoGen), or Poly(I:C) HMW (TLR3 agonist, 10 μg/mL; InvivoGen) for 24 h at 37°C prior to the assay. Conditioned cell culture supernatants were then collected and loaded for ELISA analysis.

Flow cytometry

CAR transduction efficiency was measured by detecting of the IgG hinge region using conjugated goat anti-human IgG (H + L; Jackson ImmunoResearch). To determine the target specificity of CAR19 and CAR20 NK cells, their binding to Avi-tagged CD19 or CD20 fusion proteins (ACRO Biosystems) was assessed, followed by secondary staining with fluorochrome-conjugated anti-biotin antibody. Ghost Dye Violet 450 (TONBO Biosciences) was used to determine viability, and aqua fixable viability dye (eBioscience) was used for assessing viability when fixation protocols were used. Human Fc receptor blocking solution (Miltenyi Biotec) was used to block Fc receptors and minimize non-specific staining. Phycoerythrin Fluorescence Quantitation Kit (BD Biosciences) was used according to the manufacturer's instructions to determine the number of CD19 and CD20 molecules per CAR NK cell. AccuCheck Counting Beads (ThermoFisher) were used to determine the cell concentration in each tested population. Flow cytometry analysis was performed on LSRFortessa X-20 (BD Biosciences) and data were analyzed using FlowJo (BD Biosciences). Cell sorting was performed using MoFlo XDP cell sorter (Beckman Coulter). For trogocytosis analysis, CAR cognate antigen expression was

assessed on singlet $CD56^+CD3^-GFP^-$ NK cells by flow cytometry after tumor co-culture, controlling expression levels to NK cells cultured alone (negative control) and an FMO control. Antibodies used for flow cytometry analysis include: anti-human CD45-Krome Orange (Beckman Coulter; 1:40), anti-human CD56-BV650 (Biolegend; 1:200), anti-human CD16-BV605 (Biolegend; 1:100), anti-human CD161-APC (Miltenyi Biotec; 1:100), anti-human CD161-PE (Biolegend; 1:100), anti-Biotin Tag-PE (Biolegend; 1:100), anti-human CD19-PE (Biolegend; 1:100), anti-human CD20-PE (Biolegend; 1:100), anti-human CD3-APC-H7 (Biolegend; 1:200), anti-mouse TER119-APC-H7 (Biolegend; 1:100), GFP-AF488 (Biolegend; 1:100), anti-mouse CD45-GFP (Biolegend; 1:200), Fixable Viability Dye-eFluor 506 (Invitrogen; 1:200), LIVE/DEAD Fixable Aqua Dead Cell Stain (eBioscience; 1:200), Human BD Fc Block (Miltenyi Biotec; 1:200), Biotinylated human CD19 (20–291) fusion protein (Acro Biosystems; 1:100), Biotinylated/his-tag human CD20 (1–297) fusion protein (Acro Biosystems; 1:100).

Metabolism assays

ECAR and OCR were measured in CAR NK effector cells derived from either DP or DN NK subsets using the Seahorse XF Cell Mito Stress Test Kit (Agilent), and the Seahorse XF Glycolysis Stress Test Kit (Agilent) in an Agilent Seahorse XFe96 Analyzer according to the manufacturer's protocol. The assay was performed in phenol red/carbonate-free RPMI medium (Agilent) containing 2 mM L-glutamine (Agilent), 25 mM glucose and 2 mM pyruvate (Agilent, but excluded in the glycolysis assay). Cell mito stress test was performed by examining OCRs after administering 1.5 μM oligomycin (Omy), 0.5 μM fluorocarbonyl cyanide phenylhydrazone (FCCP), 0.5 μM rotenone and antimycin A (RotA). The glycolysis test was measured as the ECAR following injection with 10 mM glucose (Glc), 1 μM Omy and 50 mM 2-deoxy-*d*-glucose (2-DG).

Tumor rechallenge assay in IncuCyte system

NK cells were co-cultured at different effector-to-target (E:T) ratios with tumor cells expressing GFP, and fresh tumor cells were added to the co-culture every 2–3 days, as previously described.[8] By the end of each rechallenge cycle, 100,000 GFP-labeled tumor cells were added. The tumor cell index represents the counts of tumor cells where the intensity of GFP fluorochrome was detected. Images of each well were captured in real time. Data were analyzed using the IncuCyte Live-Cell Imaging System.

Spheroid killing assay and TAS evaluation

Spheroids were generated by placing 10,000 GFP-labeled SKOV3 cells genetically transduced to express CD19-mCherry fusion protein ($SKOV3^{CD19-mCherry}$), or GFP-labeled SKOV3 cells as control, in 100 μL of complete McCoy's 5a Medium in each 96-well clear, round bottom, ultra-low attachment microplate (Corning, Glendale, AR). After 48 h, spheroid formation was confirmed by microscopy and CAR19 NK cells were added to spheroid-containing wells at various E:T ratios. Frames were captured with a 10× objective at 2 h intervals over the assay period. Green signal (fluorescence from GFP-expressing tumor cells) and red signal (from CD19-mCherry fusion protein) intensities were quantified using IncuCyte S3 live-cell analysis system (Sartorius). The background of each signal was determined by reference to the non-cell region under phase contrast. Areas of fluorescent positivity were outlined for each signal at a 2D section. Areas of mCherry positivity colocalized with CAR NK cells, in the absence of GFP signal, were defined as TROG-antigen Sink (TAS). For microscopy imaging analysis of CAR NK cell killing against $SKOV3^{CD19-mCherry}$ spheroids, spheroids were formed as mentioned above. Two to three spheroids were then transferred to flat-bottom plates and allowed to fully attach. CAR NK cells derived from DP subsets or mixtures including DN subsets were added to each well to cover the remaining area. DAPI staining (0.2 μM) was applied to each well to evaluate cytotoxicity intensity under each condition. Live imaging acquisition was performed using Leica DMi8 equipped with heated environmental control chamber (37°C, 5% CO_2). Images of fluorescent and bright-field channels were acquired with 20× objective. The acquired images and mosaic were processed/merged initially by LasX software from Leica. Images were saved in TIFF format and analyzed using ImageJ. For the evaluation of TAS and viability using flow cytometry, the cell mixture from each well was filtered by passing through a 20 μm filter. $CD56^+CAR^+GFP^-$ NK singlet cells from collected tubes were then analyzed by flow cytometry analysis for their mCherry positivity and L/D staining acquisition.

Single-cell cytotoxicity assay

Time-lapse imaging microscopy in nanowell grids (TIMING) was used to test NK-mediated cytotoxicity at a single-cell scale as previously described.[61] In brief, the sorted DN vs. DP- derived CAR NK cell populations and target autologous NK cells that were genetically transduced to express mCherry-CD19 fusion protein ($autoNK^{gCD19+}$) were labeled with lipophilic PKH dyes, respectively, and loaded onto nanowell arrays. The array was incubated with media that was pre-mixed with Annexin V (BD Bioscience), and monitored in real-time for 5–6 h by a Carl Zeiss Axio Observer fitted with a Hamamatsu Orca-Flash sCMOS camera using a 20 × 0.8 NA objective. Images of ~5,000 wells were collected and processed using an in-house algorithm for cell tracking and segmentation.[62]

Mass cytometry (CyTOF)

Mass cytometry was performed as previously described.[63,64] Primary antibodies were conjugated in-house with corresponding metal tags using MaxparX8 polymer antibody labeling kit following the manufacturer's protocol (Fluidigm). NK cells were washed with cell staining buffer (0.5% bovine serum albumin/PBS), and incubated with human Fc receptor blocking solution (Miltenyi Biotec) before antibody mix was added. Cells were then incubated with 2.5 μM cisplatin (Sigma Aldrich), followed by fixation and permeabilization using BD Cytofix/Cytoperm solution according to the manufacturer's protocol. For intracellular staining, cells were washed twice with perm/wash buffer and incubated directly with antibody master mix against intracellular markers. Cells were then stored

overnight in 500 μL of 1.6% paraformaldehyde (EMD Milipore)/PBS with 125 nM iridium nucleic acid intercalator (Fluidigm). To assess cells from each sample, they were washed with 1 mL of MilliQ dH_2O and filtered through a 35 μm nylon mesh (cell strainer cap tubes, BD Bioscience). The cells were then resuspended in MilliQ dH_2O supplemented with EQTM 4-element calibration beads, and subsequently acquired at 300 events/second on a Helios instrument (Fluidigm). For CyTOF analysis, antibodies used with the corresponding metal tag isotopes were included in KRT.

Mass cytometry data analysis

Mass cytometry data were analyzed using Cytobank. NK cell populations were identified by using the strategy of gating singlets in Pt194 (cisplatin)^{low} hCD45$^+$CD56$^+$CD3$^-$, for co-culture, GFP was used to facilitate the identification of targets over effector cells, and were applied to all files. CAR$^+$ and TROG-antigen expression was determined based on either isotype control or NK cells culture alone as controls. Data from 10,000 identified NK cells per each *in vitro* sample were randomly subsampled in FlowJo. Normalized data from each sample were pooled per condition and analyzed to acquire their variability in signals in Cytobank. SPADE analysis was performed for clustering and visualization of high-dimensional single-cell data. Cells with phenotypical similarity were hierarchically clustered together in subclusters (nodes) that form clusters (branches) to indicate the diverse phenotypic landscape of the data. Percentage expression was determined based on both fluorescence minus one (FMO) control and by referring to the negative cell subsets in CBMCs. The percentage and intensity expression of each marker in the clusters was transformed and normalized locally and plotted as a heatmap using Morpheus matrix visualization and analysis software (Broad Institute). Functional scores of each cluster were calculated by using the median level of relevant markers with normalization to their backgroud expression level. The maturation and homing score was calculated based on the markers NKG2A, CD16, NKG2D, EOMES, CD161, T-bet, NKp30, NKp46, NKP44, NKG2C, KLRG1, CD95, CD57, CCR6, CX3CR1, CXCR3, CXCR4, Ki67, KIRs and CD25. The activation and cytotoxicity score was calculated based on the markers 2B4, DAP12, CD8a, HLA-DR, ICOS, OX40, Zap70, Syk, CD39, CD69, CD2, DNAM-1, GranzymeA, GranzymeB and Perforin. The immune checkpoint score was calculated based on the markers TIGIT, TIM3, LAG3 and PD-1.

Xenogeneic tumor-grafted mouse models

NOD/SCID IL-2Rγnull (NSG) mice grafted with aggressive, NK-resistant tumor cells were used to examine the antitumor activity of different NK cell populations as previously described.[64,65] Tumor models included Raji lymphoma and SKOV3 ovarian cancer. All experiments were conducted in accordance with American Veterinary Medical Association (AVMA) and NIH guidelines under protocols approved by the MD Anderson Cancer Center Institutional Animal Care and Use Committee (protocol number: 00000889-RN02). Mice were maintained under specific-pathogen-free conditions, with a 12-h light/dark cycle, stable ambient temperature, and 40–70% relative humidity. For Raji mouse model, seven-week-old female NSG mice (Jackson Laboratories) were irradiated (300 cGy) on Day −1. On Day 0, 0.2×10^5 firefly luciferase-GFP labeled Raji cells were injected intravenously (i.v.). The mice were then serially treated with the indicated CAR NK cell populations via i.vi. For ovarian cancer model, seven to eight-week old female NSG mice (Jackson Laboratories) were injected intraperitoneally (i.p.) with 1×10^6 luciferase-GFP labeled SKOV3 cells seven days (Day −7) before NK cell treatment; on Day −1 the mice were irradiated (300 cGy); on Day 0 the mice were treated with the indicated NK cell populations via i.p. injection. Bioluminescence imaging was performed regularly using the Xenogen IVIS 200 imaging system (Caliper) to monitor tumor engraftment. Signal quantification (photons/second) was determined using IVIS Living Image software (Caliper Life Sciences). Mice were examined independelty by the pathologist of their reponses and safety profiles post CAR NK cells treatment.

QUANTIFICATION AND STATISTICAL ANALYSIS

Statistics

Statistical analyses were performed and plotted using Prism 10.4.0 software (GraphPad). The Student's *t* test was used to test for significance; one-way ANOVA was applied to determine the comparison among groups at a certain condition; two-way ANOVA was applied to determine the comparison among groups in a time course; *p* value for pairwise comparisons was conservatively adjusted for multiple comparisons using Bonferroni correction. Mean values ±standard error of the mean (s.e.m.) are shown. The non-linear regression model with the least trimmed sum of squares was selected as the robust goodness-of-fit.[66] Overall survival (OS) and progression free survival (PFS) analysis was calculated using Kaplan-Meier methods and compared to the treatment group using log rank tests with 95% confidence intervals (CI).